

Invited tutorial: Brillouin scattering – theory and experiment

C. WOLFF¹, M. J. A. SMITH², B. STILLER^{3,4}, AND C. G. POULTON^{5,*}

¹Center for Nano Optics, University of Southern Denmark, Campusvej 55, DK-5230 Odense M, Denmark

²Department of Applied Mathematics and Theoretical Physics, University of Cambridge, Cambridge CB3 0WA, United Kingdom

³Max Planck Institute for the Science of Light, Staudtstr. 2, Erlangen, Germany

⁴Department of Physics, University of Erlangen-Nuremberg, Staudtstr. 7, 91058 Erlangen, Germany

⁵School of Mathematical and Physical Sciences, University of Technology Sydney, NSW 2007, Australia

*Corresponding author: chris.poulton@uts.edu.au

Compiled February 15, 2021

Brillouin scattering is an important and interesting nonlinear effect involving the interaction between optical and acoustic fields in optical waveguides. It is increasingly useful in the field of photonics, where it supplies a tunable ultra-narrow linewidth response that can be used for applications including sensing, filtering, and lasing, as well as the acoustic storage of optical pulses. This tutorial gives an overview of the fundamentals of Brillouin scattering aimed at newcomers to the field, and covers the physics underlying the interaction, the mathematical theory, and setup details of foundational Brillouin experiments. © 2021

Optical Society of America

<http://dx.doi.org/10.1364/ao.XX.XXXXXX>

1. INTRODUCTION

The term *Brillouin scattering* describes an interaction in which electromagnetic waves are coherently coupled to an acoustic or mechanical wave in a light-bearing material [1–3]. Brillouin scattering differs from “standard” opto-acoustic interactions (such as those occurring in surface acoustic wave devices and acousto-optic modulators) in that the optical beams can themselves excite or influence the acoustic field. This complexity of interaction results in a number of effects: an acoustic wave can be generated from the thermal background of the waveguide material, an existing acoustic wave may be depleted by an optical pulse, or a feedback loop known as *stimulated Brillouin scattering* (SBS) can arise, manifesting as a third-order optical nonlinearity several orders of magnitude stronger than the Raman or Kerr effect. The Brillouin effect possesses an extremely small linewidth — typically from tens to hundreds of MHz, and is often also tunable over a large frequency range. Such an extremely narrow-band nonlinearity has found many useful applications in modern photonics (for a recent review see [4]): the narrow spectral line can be used as a filter in microwave photonics experiments [5, 6], or as a source of gain in a Brillouin laser [7, 8]; the dependence of the Brillouin frequency shift on the speed of sound makes the response suitable for sensing, especially of material properties [9, 10]. The innate directionality of the Brillouin process can be used as a basis for non-reciprocal effects [11, 12], and the interaction between light and sound can be used to create an acoustic “memory”, in which information is transferred to the relatively long-lasting acoustic waves [13, 14].

The aim of this tutorial is to consolidate the current tools, as well as the conceptual foundations, needed to understand, model, and experimentally demonstrate Brillouin scattering in modern nanophotonics experiments. In addition to discussing the underlying physics of Brillouin processes, we present the governing equations for Brillouin interactions (including new, comprehensive derivations of these equations), and we discuss the solution of these equations in several of the more important situations that arise in practice, such as in the dynamics of interacting pulses. We also outline the experimental configurations of the most commonly-used Brillouin measurements. At each stage we explain the physics and modelling of these interactions and explore the range of applicability for the various approximations that are often made.

There have been several recent review and tutorial articles covering Brillouin scattering in modern photonics. An overview of experimental structures and applications of Brillouin scattering in modern nanophotonics can be found in [4]. A discussion on platforms and the formal relation with opto-mechanics can be found in [15]. A comprehensive recent tutorial on Brillouin gain in both waveguides and resonators can be found in [16]. Readers interested in the theory of Brillouin scattering in optical fibres are directed to the excellent review by Kobayakov *et al.* [17]. Finally, we have found that a very good introduction to the theory of elasticity for researchers with an electromagnetics background is the book by B.A. Auld [18]. It is our aim here to bring together the main concepts and tools from these publications, together with additional material on numerical

and experimental methods for practical Brillouin modelling and measurement, in a way that makes Brillouin scattering readily accessible to graduate students and newcomers to the field.

This tutorial has been organised as follows: in Section 2 we describe the underlying physics of the Brillouin interaction and classify the different types of scattering that may arise. In Section 3 we give a general derivation of the equations that describe Brillouin interactions; we also give commonly-used approximations for these equations. In Section 4 we discuss the materials and platforms that are necessary for harnessing Brillouin interactions in modern photonics systems. In Section 5 we describe several important Brillouin experiments, including details on how these can be set up and how the results can be modelled using the equations in the previous section. We conclude with some further reading on important aspects of Brillouin scattering that we have not covered in this tutorial. The Appendix contains details on numerical computation of optical and acoustic modes, and how these can be used to calculate useful quantities such as the Brillouin gain.

2. PHYSICS OF BRILLOUIN SCATTERING

We consider an optical waveguide, oriented along the z axis and considered to be infinitely long (see Fig. 1a). Provided that the refractive index of the waveguide is greater than the surrounding material, this structure will support confined optical modes with a given angular frequency ω (with $\omega = 2\pi f$, where f is the optical frequency), and wave number k . These modes, together with their associated modal fields, may be determined using a variety of numerical methods, all of which solve Maxwell's equations on the cross section with appropriate boundary conditions on the edge of the computational domain (such boundary conditions should emulate an unbounded domain, from which no reflections occur and which have any evanescent fields decreasing away from the waveguide, and can be numerically implemented using a perfectly-matched layer [19]). It is possible to solve for the modes in terms of either ω or k , with the choice depending on the specific details of the numerical formulation.

Depending on the material composition (see Section 4), waveguides can also support *confined acoustic modes*¹ [18], with angular frequency Ω (with $\Omega = 2\pi v$, where v is the acoustic frequency) and acoustic wave number q . Unlike electromagnetic waves, which are always “transverse” in the sense that they can be represented by the curl of a divergence-less vector, the elastic field equations support an additional set of “longitudinal” waves — pressure waves — which correspond to pure compressions and dilatations of the material. Any acoustic wave can be decomposed into one pressure and three shear components, with each shear component representing a mechanical wave with motion transverse to one of the coordinate axes. The pressure waves are given by the diagonal components of the mechanical strain tensor \mathbf{S} , whereas the shear components are given by the off-diagonal terms: for the pressure wave propagating in the z direction in Fig 1a the dominant component of the strain is given by S_{zz} , and for the breathing mode depicted in Fig. 1b the dominant component is S_{xx} . Pressure waves have a higher velocity than shear waves, in most photonic systems by a

¹We note here that although the terminology “acoustic field” or “acoustic wave” is often used in this context, these waves are often mechanical waves in solids, and so can support both shear and pressure waves, as well as waves that are mixtures between the two, such as Rayleigh or surface waves. Here we follow the common usage in referring to the ‘acoustic’ and ‘optical’ waves when discussing the physics of the wave interaction, and the ‘electromagnetic’ and ‘elastic’ fields when discussing the relevant underlying interactions and field components.

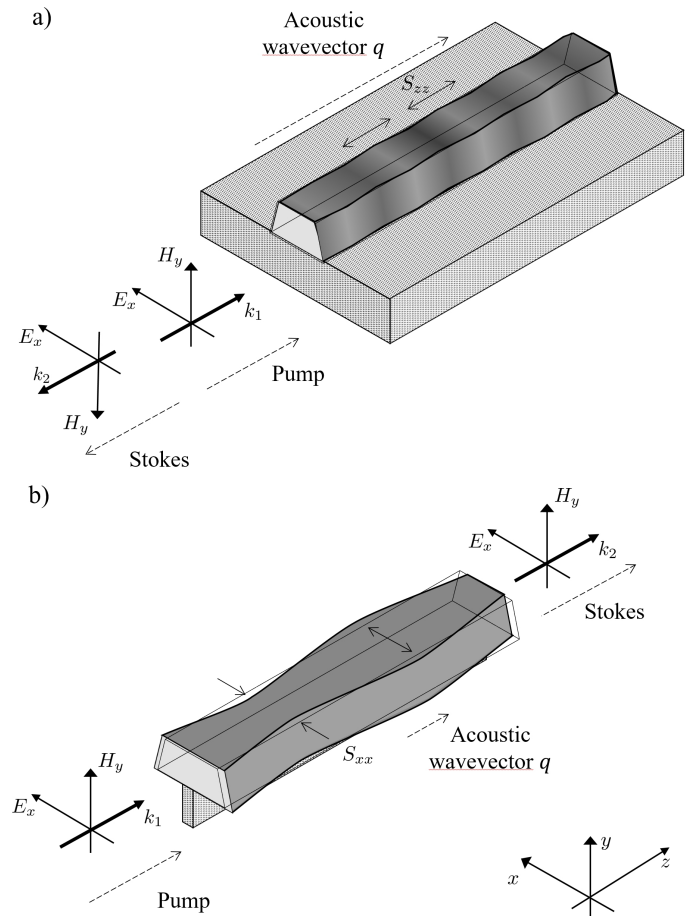


Fig. 1. Representative geometries of Brillouin nanophotonic waveguides, in which the pump is input at $z = -\infty$ and travelling in the positive z direction. a) In backward Brillouin scattering the pump and Stokes waves propagate in opposite directions. In this case the acoustic mode can be confined when the waveguide core lies on a substrate: the acoustic mode consists mostly of pressure waves moving along the waveguide, and so the dominant strain component of the acoustic mode is S_{zz} , meaning that any leakage from the core is in the form of shear waves, which are below cutoff in the substrate. b) In forward Brillouin scattering, the pump and Stokes are co-propagating. The acoustic wave propagates in the direction of the pump, but with a very small wave number. The dominant strain component of the acoustic field (S_{xx}) corresponds to vibrations that are transverse to the waveguide axis, and so the waveguide core must typically be suspended to prevent coupling to substrate pressure waves.

factor of 1.5-2. In real waveguides, these components are almost always coupled on physical boundaries, and so any particular acoustic mode will be a mix of pressure and shear waves, with one or the other dominating (see the waves in Fig. 1). This mixing can form surface waves, of which Rayleigh waves are the particular form if the surface is free to vibrate, as occurs if a solid borders vacuum or (to a good approximation) air. Rayleigh waves are even slower than shear waves, with a velocity about 90% of the shear wave velocity in most photonic materials.

Acoustic waves can be confined to a waveguide either by total-internal-reflection (TIR), or by a strong impedance mis-

match between the core and the cladding. The conditions for confinement of an acoustic wave by TIR are a little more complicated than those for optical waves, but the same underlying physics applies: the wave speed within the core should be less than outside. Acoustic TIR guidance arises in two regimes. The first is where the core wave speed is slower than *all* acoustic modes in the cladding. This is the true TIR regime, where no energy can be transferred to cladding modes. If the optomechanically active mode in the core is a pressure wave (as is common in backward Brillouin), this requires a relatively strong mechanical contrast, because it needs to be slower than the shear waves in the cladding, which are typically about 30–50% slower than the pressure cladding waves. If the core wave is faster than the cladding shear wave, energy can be lost to the latter. However, the efficiency of converting core pressure into cladding shear grows with the mechanical contrast of the two materials. This leads to the second regime: if the core is just very slightly softer or denser than the cladding, there can exist pressure-type core waves with negligible loss of energy to cladding modes. For standard optical fibres, the germanium doping in the core reduces the sound velocity sufficiently that a guided pressure wave, of about the same diameter as the optical mode, can form [17]; at the same time, the mechanical contrast is low enough that almost no energy is lost to the shear waves. For high-contrast combinations of materials, the interfaces between the different solids can cause coupling from pressure waves to shear waves, and the situation becomes more complicated: the core must be considerably softer than the cladding to confine a mode with a dominantly pressure-wave component. If TIR confinement is not possible (as is almost always the case for forward Brillouin scattering), the acoustic wave can be confined by a very strong mismatch in acoustic impedance between the core and the cladding, thereby preventing acoustic waves from carrying energy away from the core. Typically this is achieved by suspending the core in air. The elastic waveguide modes and their associated frequencies can be computed in the same manner as for the electromagnetic modes, substituting the equations of linear elasticity for Maxwell's equations (see Appendix A).

The fundamental nature of the Brillouin interaction can be described as follows: interference between optical modes of a waveguide generates a pressure, or a force density, on the material, arising from radiation pressure or electrostriction (see below). This pressure then excites an acoustic wave, provided that energy and momentum are conserved in the interaction. In turn, the strains of the acoustic field change the dielectric properties of the medium and perturb its boundaries, effectively creating a grating which scatters light from one optical mode to another. The result (see Fig. 2) is a narrow spectral line that is shifted away from the pump by a frequency equal to the frequency Ω of the acoustic wave — this difference is known as the *Brillouin shift*. The specific value of Ω is determined by the frequency of the pump and by the material parameters of the acoustic wave (see Section 2.B), and can range from the hundreds of MHz (for forward Brillouin scattering) to tens of GHz (for backward Brillouin scattering). The width of the Brillouin spectral line is determined by the lifetime of the phonon mode. For typical materials and waveguide configurations this is of the order of 1–10 ns, giving a linewidth in the tens to hundreds of MHz.

In optically isotropic material platforms, there are four leading-order physical mechanisms that lead to the opto-

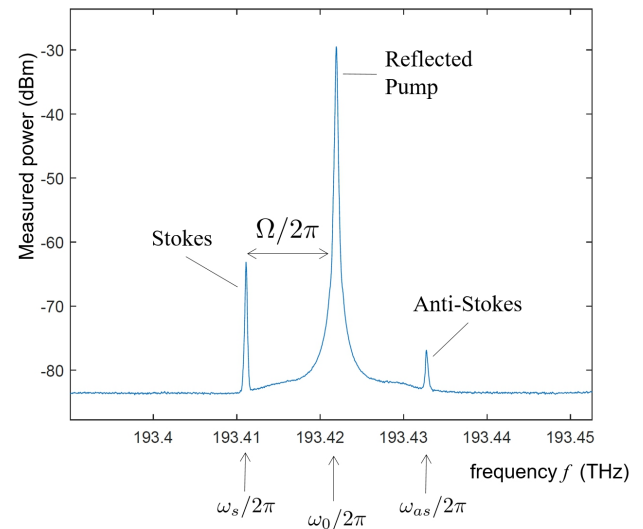


Fig. 2. Experimental measurement of a backward Brillouin scattering spectrum, showing the Stokes and anti-Stokes lines, as well as the reflection from the pump. This experiment used 300m of silica single-mode fibre, at levels of pump power ($\sim 100\text{mW}$) where the Stokes begins to dominate but where the anti-Stokes is still visible.

acoustic interaction described above². First, mechanical strains in the waveguide can be induced by the electromagnetic field via electrostriction. Related to electrostriction is the converse effect of photo-elasticity, whereby strains induce local changes in the dielectric permittivity. Third, radiation pressure arising from the reflection of electromagnetic waves from structural boundaries can physically move the waveguide boundaries and so drive acoustic waves. Finally, the motion of structural boundaries induced by mechanical vibrations induces a localised change in the electromagnetic properties. The two quantities electrostriction and photoelasticity are related via a Maxwell relation [23, 24], as are the moving boundary and radiation pressure effects. This relationship between “back-action” — where the electromagnetic field exerts forces on the mechanical structure, and what might be described as “forward action” — where a change in dielectric properties leads to scattering of light, can be derived from conservation of energy at the microscopic scale: the work needed to deform a structure must be balanced by the change in the amount of energy contained in the electromagnetic field, and any work done by the electromagnetic field must result in a commensurate change in the elastic energy.

A. Stokes and anti-Stokes transitions

As in any macroscopic field interaction, we can also picture Brillouin processes in terms of the creation and annihilation of quasi-particles, in this case photons (which give rise to the electromagnetic field) and phonons (which in the classical limit form material vibrations in the waveguide). It is often useful to distinguish interactions according to whether the phonon is absorbed or emitted in the interaction (see Fig. 3). In the *Stokes* Brillouin

²For completeness we note that acoustic fields generate both strains and rotations, which drive Brillouin scattering via photoelasticity (electrostriction) and roto-opticity (electroevolution), respectively [20]. However, roto-optic effects are usually only significant in waveguides made from materials with strong optical anisotropy and will therefore not be discussed in detail in this introductory tutorial [21, 22]

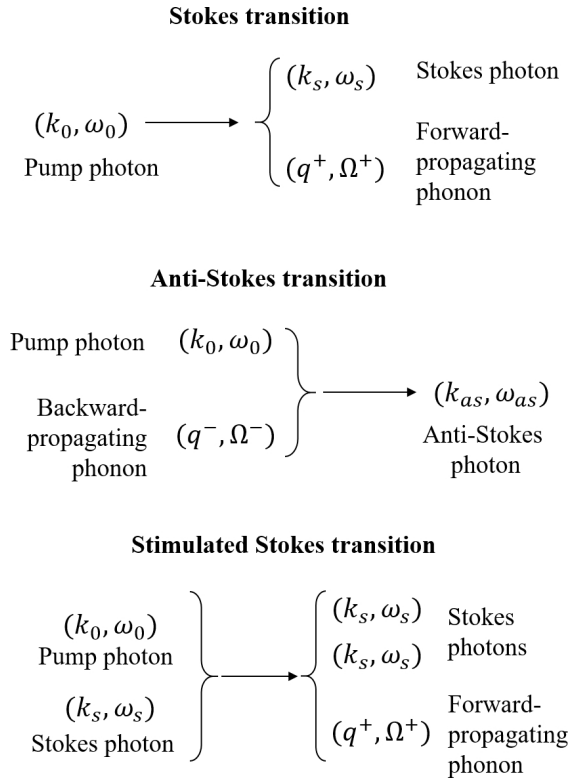


Fig. 3. Different transitions in Brillouin scattering. Each photon is associated with a wave number k and frequency ω . Each transition can be visualised as a closed set of vectors located in the dispersion diagrams of Figs 4-6.

transition, a high-frequency photon is converted into a lower frequency Stokes photon, in the process creating a phonon. This transition can be either stimulated or can occur spontaneously – in the case of spontaneous emission, this refers to emission that arises due to the existence of thermal phonons³. The Stokes transition is the one most commonly used in backward Brillouin scattering experiments. *Anti-Stokes* transitions, in which a lower frequency photon (typically the pump) is converted to a higher-frequency photon (the anti-Stokes), while absorbing a phonon, are also possible. Both processes can be seen at work in, for example, Brillouin memory experiments [14], in which the Stokes process is used to “write” information to the acoustic field and the anti-Stokes process is used to “read” it back out. The exact conditions for when these processes become stimulated, and indeed whether stimulated scattering is possible, arise from consideration of the coupled mode equations in Section 3.

B. Phase matching and the main types of Brillouin scattering

Both Stokes and anti-Stokes processes must obey conservation of energy and momentum. Brillouin coupling between two optical waves with frequencies and wave numbers given by (k_1, ω_1) and (k_2, ω_2) therefore requires an acoustic wave with wave number q and frequency Ω given by

$$q = k_2 - k_1, \quad \text{and} \quad \Omega = \omega_2 - \omega_1. \quad (1)$$

³In the context of Brillouin scattering, “spontaneous emission” of photons refers to any incoherent emission, be it true spontaneous emission due to phononic vacuum fluctuations or emission stimulated by pre-existing thermal phonons. Above a low threshold temperature $T \approx \hbar\Omega/k_B \approx 1\text{K}$, the latter contribution dominates by far.

This reflects the highly resonant nature of the process: minor deviations on the scale of the mechanical quality factor lead to a rapid reduction of the nonlinear interaction. The equations (1) are the phase matching conditions between the interacting waves, and can be represented graphically on a dispersion diagram, as shown in Fig. 4a and Fig. 5a. On these diagrams a phase-matched interaction has the property that the vectors of all three waves add to zero. The relations (1) and their associated dispersion diagrams are important for understanding the direction of propagation, and also give a good indication of the sorts of approximations that can be made to predict system behaviour.

In general there are three main types of Brillouin scattering in waveguides, and we outline their main features in the following.

B.1. Backward Brillouin scattering

In backward Brillouin scattering, counter-propagating optical beams exchange energy via an acoustic mode whose wave vector is oriented in the propagation direction of the pump for the Stokes process, and in the opposite direction to the pump in the anti-Stokes process (see Fig 4a). Because this requires an acoustic mode with a large wave vector in the waveguide direction, these modes are, in the core of the waveguide, usually very close to being pure pressure plane waves, with phase fronts aligned normal to the waveguide axis. Given the difference of several orders of magnitude in frequency between light and sound waves, an excellent approximation for the phase matching condition for backward Brillouin scattering is that the acoustic wave number is twice as large as the optical wave number, leading to an approximation of the Brillouin shift of

$$\Omega \approx 2k_0c_p, \quad (2)$$

where c_p is the phase velocity of the acoustic wave and k_0 is the wave number of the pump. For waveguides that have cross-section dimensions larger than the optical and acoustic wavelength in the core, the dominant strength of the backward interaction is determined by the electrostrictive/photoelastic effect. This is because the strains of the acoustic field do not perturb the waveguide boundaries, and conversely, radiation pressure from the optical field does not easily excite longitudinal acoustic modes (it is worth noting that this may not be the case for waveguides with strongly guided acoustic modes, in which pressure and shear modes become strongly hybridized). Because for these waveguides the dominant electromagnetic field components are aligned transverse to the direction of propagation (say, to the y axis), and the largest elastic field components are aligned along the waveguide (z -axis), the electrostrictive coupling is typically determined by the p_{yyzz} component of the Pockel’s tensor (see Section 3.C); in contracted notation this is denoted p_{23} , which is equal to p_{12} in isotropic and cubic materials and the coefficient usually given in SBS computations.

B.2. Forward Brillouin scattering

In forward Brillouin scattering, co-propagating optical waves couple to an acoustic mode that has a finite frequency but a wave vector that is close (but not exactly equal) to zero (see Fig. 5a). Such an acoustic mode is therefore very close to being *transverse*, in the sense that the mode possesses a very small group velocity and a finite, non-zero phase velocity. This means that very little energy is transported along the waveguide direction; for conventional waveguides (i.e. those that are translationally invariant, as opposed to periodically modulated) the dominant

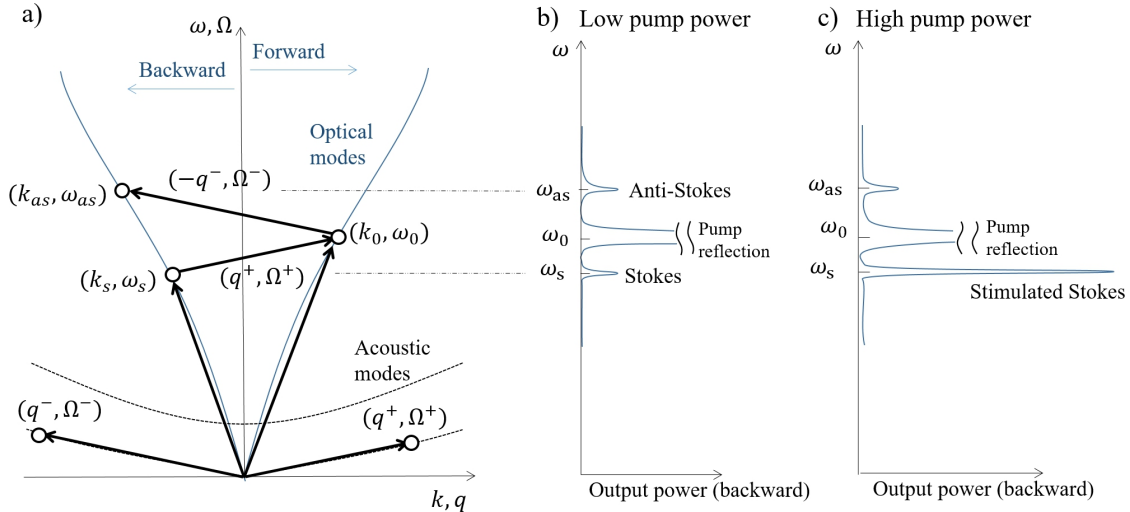


Fig. 4. a) Sketch of a dispersion diagram for backward Brillouin scattering, showing both Stokes and anti-Stokes transitions. Note that in reality the steepness of the optical mode bands, or light lines, (solid blue) would be far greater than is depicted, and the frequency of the acoustic mode bands (dashed black) would be far lower. b) Illustration of output power on a detector in the backward direction, in the case of low pump power. For low pump power both the Stokes and anti-Stokes signals are visible. In most experiments there exists a reflection, usually from the input facets of the waveguide, from the pump. c) Illustration of output detector power in the backward direction for high pump powers. As the pump power increases the Stokes becomes stimulated and dominates over the anti-Stokes signal (as shown in the measured spectrum of Fig. 2).

components of the strain field are therefore those transverse to the waveguide orientation.

In order to properly confine these almost-transverse acoustic modes, a waveguide must be isolated as much as is practicable from its surroundings, that is, we must create a large enough impedance mismatch so that the acoustic mode cannot escape from the core. Such isolation can be achieved effectively by suspending the waveguide (or its surrounding substrate) in air [25, 26], supporting the waveguide on a very thin pillar [27], or trapping the acoustic mode in a photonic crystal fibre [28] or using a phononic crystal [29]. The frequency of the acoustic mode in forward Brillouin scattering depends strongly on the physical dimensions of the waveguide, for example, the angular frequency of the first “breathing” mode of a rectangular waveguide is on the order of

$$\Omega \approx \frac{\pi}{a} \sqrt{\frac{E}{\rho}}, \quad (3)$$

where a is the waveguide width, E is the Young’s modulus and ρ is the material density of the core. This is usually a good approximation for the forward Brillouin frequency shift. Since these transverse acoustic modes are highly dependent on the waveguide dimension, this type of scattering was initially called “Guided acoustic wave Brillouin scattering”, or GAWBS [30]. In forward Brillouin scattering the acoustic modes possess strain components that are dominantly transverse to the waveguide axis, and so the electrostrictive interaction is typically determined by the p_{yyyy} or p_{22} (or p_{11} for cubic and isotropic symmetry) component of the Pockel’s tensor. The coupling can also be strongly enhanced through radiation pressure, which can act in the same direction as the strain field [25].

Forward Brillouin scattering has much in common with Raman scattering, and is indeed referred to as “Raman-like Brillouin scattering” [28]. Like Raman scattering, forward Brillouin scattering couples two optical beams to a vibration that

is “stationary” — in Raman scattering this is either the localised acoustic mode associated with a molecular vibration, or a high-frequency, non-propagating vibrational mode of a lattice (known as the optical phonon band because of its ability to couple to light). Unlike Raman scattering, which involves scattering from vibrations at the molecular scale, forward Brillouin scattering involves scattering from elastic waves that are sufficiently long so that the molecular or atomic structure of the material can be considered to be a continuum; these waves therefore consist of collective movement of atoms arising from the lower frequency “acoustic” phonon band of the material. The frequencies of forward Brillouin scattering are therefore approximately 4 orders of magnitude lower than that for Raman scattering, lying in the hundreds of MHz rather than in the THz range.

B.3. Inter-modal Brillouin scattering

Intermodal Brillouin scattering involves coupling between different order optical modes in a multi-moded waveguide (see Fig 6a,b). This process can occur in either the forward or backward direction, with each case having analogous properties to the standard forward or backward Brillouin configurations. Because the exchange of energy is between optical modes with potentially different symmetry, it is important that the acoustic mode possesses the correct symmetry to support the interaction [31]. In the simple case of a step-index fibre or a suspended rectangular semiconductor waveguide, the different optical modes are simply the different polarization states that can propagate. In more complex geometries such as a micro-structured fibre this simple correspondence breaks down and a full modal picture is necessary. An outline of the symmetries and allowed transitions for waveguides with C_{2v} symmetry is given in Fig. 6c; a more comprehensive discussion can be found in Ref. [31].

C. Initiation of Brillouin scattering

Brillouin processes can be initiated either through the action of an optical *seed*, i.e. a small amount of power from a sec-

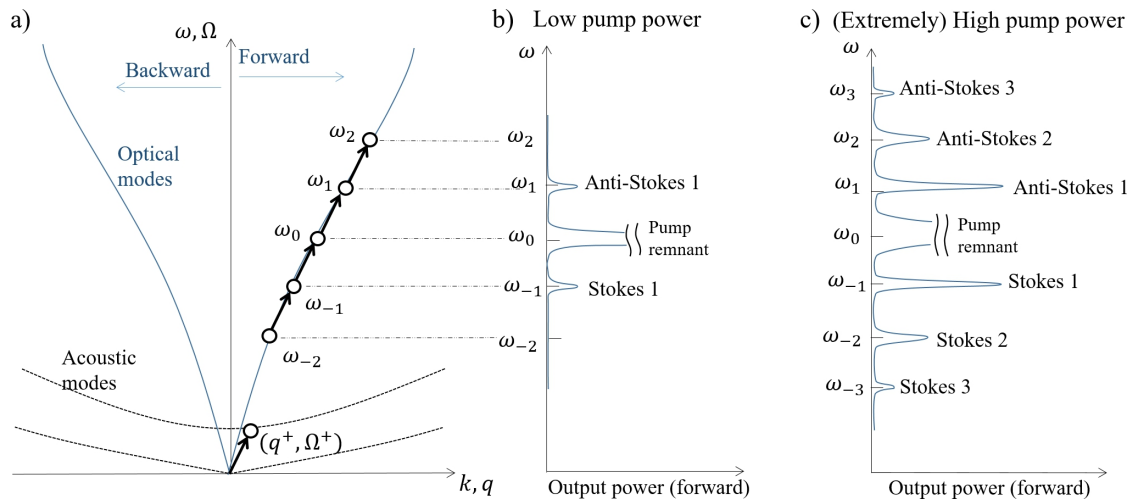


Fig. 5. a) Sketch of a dispersion diagram for forward Brillouin scattering, showing the set of Stokes and anti-Stokes transitions up to the second order. All transitions use the same acoustic mode. b) Illustration of output power on a detector in the forward direction, in the case of low pump power. For low pump power both the Stokes and anti-Stokes signals are visible, with the higher orders typically hidden in the noise floor. Because the pump also propagates in the forward direction it will feature extremely strongly in the detected power and usually must be filtered out. c) Illustration of output detector power in the forward direction at very high pump powers. As the pump power increases the first order Stokes/anti-Stokes begin to combine with the existing acoustic modes to form higher order lines.

ondary optical field at the Stokes frequency (the Stokes beam), or through the action of thermal phonons in the waveguide that scatter the pump. Experiments can therefore be divided into *seeded* and *spontaneous* Brillouin measurements. The difference is seen in the experimental setup for backward Brillouin scattering in Fig. 7: the seeded experiment includes an input Stokes wave downshifted from the pump by the Brillouin frequency shift, whereas the spontaneous experiment requires only the pump. Both cases are “driven”: seeded experiments require an additional externally-applied optical field, while the spontaneous interactions are initiated by thermal fluctuations.

While there is broad agreement on the meaning of a spontaneous Brillouin measurement, there is some division in the literature over the exact meaning of *stimulated* Brillouin scattering, and it is useful to clarify this point. Here and in the following discussion we take “stimulated” to refer to any process whereby the Stokes beam can experience gain if all sources of loss are removed from the system, after the system has achieved steady state. For example, under this definition backward Brillouin scattering is always a stimulated process, even if it is initiated spontaneously. As we shall see in Sec. 3, forward Brillouin scattering is not a stimulated process, since in the steady state the Stokes and anti-Stokes lines periodically exchange energy, such that neither experiences a net gain.

3. THE BRILLOUIN COUPLED MODE EQUATIONS

Although Brillouin scattering can in principle occur in any kind of photonic component, it is typically encountered in waveguides. Until fairly recently, most research had been conducted in step-index fibres and this is still reflected to some degree in the presentation of Brillouin scattering in textbooks. This leads to several approximations that have become widespread in the discussion of Brillouin effects; for example: Brillouin scattering is commonly characterized by an intensity gain coefficient (in units of m/W), which is considered an intrinsic material parameter. This approximation only holds as long as the optical and

acoustic waves are almost unperturbed plane waves. When the mode profiles differ from this (e.g. in structured fibres or nanoscale waveguides), a description based on the full eigenmodes becomes necessary and the notion of an “SBS-gain” becomes strongly dependent not only on the waveguide geometry but the participating modes, unless it breaks down altogether as in the case of forward Brillouin scattering.

A first-principles calculation of Brillouin scattering, e.g. by solving Maxwell’s equations nonlinearly coupled to the Christoffel equation, is impossible in virtually every system of practical relevance. This is due to a separation of scales: first, the time scales of the optical and the acoustic problems differ by typically five orders of magnitude. Second, even integrated waveguides with record-breaking gain coefficients require interaction lengths on the millimeter scale to provide appreciable overall response; i.e. the system size differs from the acoustic wave length by some four orders of magnitude. This separation of scales makes a coupled-mode description particularly well-suited to Brillouin problems.

A. Length scales of Brillouin scattering

We first discuss the relevant length and time scales in a typical Brillouin problem. There are four relevant length scales, which we can roughly sort in ascending order: the fundamental length scale is the optical wavelength λ in the waveguide. We stress that this differs from both the wavelength in vacuum and that in bulk matter. It is most easily expressed via the optical wave number $k = 2\pi/\lambda$, which is typically found via numerical calculation alongside the optical mode profile e.g. in the form of a mode index. The optical wavelength λ is of the order of hundreds of nanometers — most recent Brillouin experiments take place in the near infrared and so this quantity usually ranges from 500 nm to 1 μm .

The next potentially relevant length scales are the acoustic wavelength and localization length. The acoustic wavelength is given by the wave number difference of the optical modes

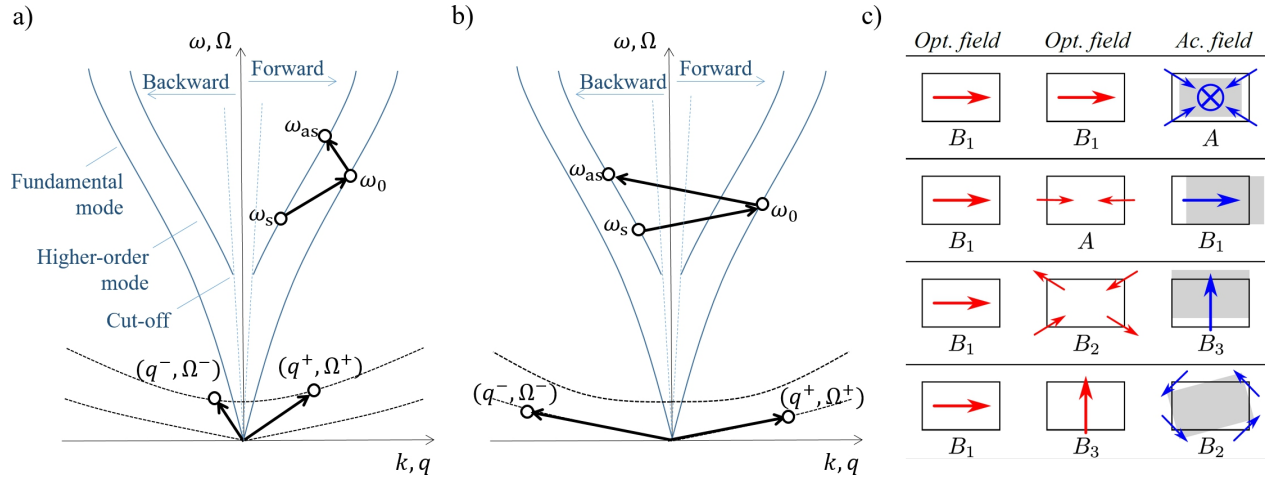


Fig. 6. Forward (a) and backward (b) dispersion diagrams for intermodal Brillouin scattering. In the cases illustrated the Stokes and anti-Stokes lines result from phonons propagating in opposite directions, as in the backward case. The particular acoustic mode that enables the intermodal transition depends on the symmetries of both optical modes. c) Combinations of optical and acoustic fields that have non-trivial photoelastic contributions in isotropic rectangular waveguides (or more generally, waveguides with C_{2v} symmetry) where arrows denote polarization directions and A, B_j denote the mode characters. Reproduced with permission from [31].

(see Figs. 4–6), where backward propagating modes have negative wave number k . For example: If the optical wave numbers of two forward propagating modes differ by 10%, then the relevant acoustic mode for this inter-mode process will have a wavelength ten times greater than the optical wavelength. This means that in every backward Brillouin scattering and some forward inter-modal problems, the acoustic wavelength is of a similar order to the optical wavelength. The acoustic localization length is the length over which a sound wave of frequency Ω decays. It is linked to the acoustic wavelength via the quality factor (typically a few 100) and typically takes values of several dozen to hundreds of microns. It should be noted that in intra-mode and most inter-mode forward scattering settings the acoustic wavelengths can reach the order of centimeters or even meters; due to the low acoustic group velocity the localization length can often remain sub-millimeter in forward scattering as well. Therefore, the most appropriate second length scale is almost always the acoustic localization length, which we denote as the inverse acoustic damping coefficient $1/\alpha_b$.

The third relevant length scale is that on which the waveguide varies *along* the direction of propagation. In the case of a fibre, this is simply its length; in nano-scale waveguides this can be e.g. the distance between suspension posts, sharp bends or similar features. We will denote this with L_{wg} . This parameter describes how far optical and acoustic waves can travel without being perturbed by a waveguide discontinuity.

The last relevant length scale is the length scale of the optical signal L_{sig} . Examples for this are the distance over which SBS amplifies a weak signal or the spatial length of the optical pulses that are injected. Unlike the previous three lengths, this one depends strongly on both the shape of the optical excitation (e.g. pulse width) as well as the incident power level. The basic idea of a coupled mode model is to describe the system using functions that vary on the length scale of the optical signals. Simply as a matter of efficiency, in many cases (e.g. in applications such as lasing and filtering) this will be comparable to the waveguide length. However, this is not necessarily the case e.g. in storage and sensing experiments, nor is the waveguide length

necessarily equal to the length scale L_{wg} .

Finally, we would like to mention two length scales that in our experience are less impactful for the formulation of coupled mode equations. The first is the optical decay length. This quantity is usually at least comparable to the waveguide length in order to ensure that signals can actually pass through the system. The final length scale is the size of the waveguide perpendicular to the direction of propagation. This length is not relevant for the formulation of the coupled mode equations, however it can allow for approximations e.g. to the participating modes or the acoustic frequency as in Eq. (3).

B. Fundamental approximations and coupled mode equations

The main approximation that is needed to derive the coupled mode equations is to decouple the transverse coordinates x, y from the direction of propagation z and time. To this end, we express the optical and acoustic fields as waveguide eigenmodes (composed of the transverse field profiles and the harmonic z, t -dependence) weighted by one complex-valued envelope function $a_n(z, t)$ per contributing optical mode and $b(z, t)$ for the acoustic field:

$$|\psi(x, y, z, t)\rangle = \sum_n a_n(z, t) |\Psi_n(x, y)\rangle e^{ik_n z - i\omega_n t} + \text{c. c.}, \quad (4a)$$

$$|\phi(x, y, z, t)\rangle = b(z, t) |\Phi(x, y)\rangle e^{iqz - i\Omega t} + \text{c. c.}, \quad (4b)$$

where c. c. represents complex conjugate terms, n labels the optical modes, k_n and q are the optical and acoustic wave numbers, ω_n and Ω the optical and acoustic frequencies, and $|\psi\rangle = [\mathbf{E}, \mathbf{H}]^T$ and $|\phi\rangle = [\mathbf{T}, \mathbf{V}]^T$ denote the optical and acoustic states, respectively. In essence, Eq. (4) is just the familiar separation of variables ansatz for solving partial differential equations, however please note that we have not made any statement as to how well the expansions Eq. (4) satisfy Maxwell's equations and the equations of linear elasticity at this point. Generally, the applicability of such a modal expansion requires the amplitudes (here: a_n and b) to vary slowly compared to the respective carriers $\exp(ik_n z - i\omega_n t)$ and $\exp(iqz - i\Omega t)$. With reference to

the length scales discussed in Section 3.A, this means that we require

$$\lambda \ll L_{\text{sig}}, \quad (5)$$

to make an ansatz like Eq. (4) in the first place. If the expansion is assumed to be complete, all the field information (for example the optical polarization) at each point of the waveguide is contained within the expansion coefficients $a_n(z, t)$ and $b(z, t)$.

In addition to the coupled mode expansion, we also make a few more approximations in order to keep the derivations concise. Primarily, we ignore dispersion – both waveguide and material dispersion – in the derivation. Generally in Brillouin computations dispersion plays a very small role, because the Brillouin shift is so small that the change in mode index over this range can be safely neglected. An example for how to include dispersion can be found here [32, 33].

B.1. Optical mode equations

We begin with Maxwell's equations

$$\nabla \times \mathbf{E} = -\partial_t \mathbf{B}, \quad (6a)$$

$$\nabla \times \mathbf{H} = \partial_t \mathbf{D} + \mathbf{J}, \quad (6b)$$

where \mathbf{D} and \mathbf{B} are the electric and magnetic induction fields, respectively, \mathbf{E} and \mathbf{H} are the electric and magnetic fields, respectively, \mathbf{J} is the dissipative current due to Ohmic losses and ∇ is the three-dimensional del operator. Introducing the constitutive expansions $\mathbf{B} = \mu \mathbf{H}$, $\mathbf{D} = \epsilon \mathbf{E} + \mathbf{P}^{\text{NL}}$, and $\mathbf{J} = \sigma \mathbf{E}$, and decomposing the del operator into transverse and longitudinal components $\nabla = \nabla_{\perp} + \hat{\mathbf{z}} \partial_z$, the Maxwell's equations above become

$$\nabla_{\perp} \times \mathbf{E} + \hat{\mathbf{z}} \times \partial_z \mathbf{E} = -\partial_t (\mu \mathbf{H}), \quad (7a)$$

$$\nabla_{\perp} \times \mathbf{H} + \hat{\mathbf{z}} \times \partial_z \mathbf{H} = \partial_t (\epsilon^{(R)} \mathbf{E}) + \partial_t \mathbf{P}^{\text{NL}} + \sigma \mathbf{E}, \quad (7b)$$

where $\hat{\mathbf{z}} = (0, 0, 1)$, \mathbf{P}^{NL} denotes the nonlinear polarization field, and $\epsilon^{(R)}$, σ and μ denote the real part of the total permittivity, the (real-valued) Ohmic conductance and permeability of the medium, respectively. For reference, the real permittivity and conductance can be combined into a complex permittivity as usual: $\epsilon = \epsilon^{(R)} + i\sigma/\omega$ when transforming to the frequency domain. Rearranging Eq. (7) and assuming an absence of nonlinear magnetic effects, we write that $\mathbf{P}^{\text{NL}} = \Delta \epsilon \mathbf{E}$ with a perturbation $\Delta \epsilon$ that, unlike $\epsilon^{(R)}$, depends on both time and on the position z along the waveguide, to obtain

$$\begin{aligned} \mathbb{E}^{(\text{opt})} \partial_t \begin{pmatrix} \mathbf{E} \\ \mathbf{H} \end{pmatrix} + \mathbb{P}^{(\text{opt})} \partial_z \begin{pmatrix} \mathbf{E} \\ \mathbf{H} \end{pmatrix} + \mathbb{D}^{(\text{opt})} \begin{pmatrix} \mathbf{E} \\ \mathbf{H} \end{pmatrix} \\ = -\partial_t \left[\Delta \mathbb{E}^{(\text{opt})}(t) \begin{pmatrix} \mathbf{E} \\ \mathbf{H} \end{pmatrix} \right] - \mathbb{S}^{(\text{opt})} \begin{pmatrix} \mathbf{E} \\ \mathbf{H} \end{pmatrix}, \end{aligned} \quad (8)$$

where

$$\begin{aligned} \mathbb{E}^{(\text{opt})} &= \begin{pmatrix} \epsilon^{(R)} & 0 \\ 0 & \mu \end{pmatrix}, \quad \mathbb{S}^{(\text{opt})} = \begin{pmatrix} \sigma & 0 \\ 0 & 0 \end{pmatrix}, \quad \Delta \mathbb{E}^{(\text{opt})} = \begin{pmatrix} \Delta \epsilon & 0 \\ 0 & 0 \end{pmatrix}, \\ \mathbb{P}^{(\text{opt})} &= \begin{pmatrix} 0 & -\hat{\mathbf{z}} \times \\ \hat{\mathbf{z}} \times & 0 \end{pmatrix}, \quad \mathbb{D}^{(\text{opt})} = \begin{pmatrix} 0 & -\nabla_{\perp} \times \\ \nabla_{\perp} \times & 0 \end{pmatrix}. \end{aligned} \quad (9)$$

Introducing the notation $|\psi\rangle = [\mathbf{E}, \mathbf{H}]^T$ the system Eq. (8) takes the more compact form

$$\begin{aligned} \mathbb{E}^{(\text{opt})} \partial_t |\psi\rangle + \mathbb{P}^{(\text{opt})} \partial_z |\psi\rangle + \mathbb{D}^{(\text{opt})} |\psi\rangle \\ = -\partial_t [\Delta \mathbb{E}^{(\text{opt})} |\psi\rangle] - \mathbb{S}^{(\text{opt})} |\psi\rangle. \end{aligned} \quad (10)$$

Next we implement the expansion Eq. (4a) of the optical fields:

$$|\psi(x, y, z, t)\rangle = \sum_n a_n e^{i\phi_n(z, t)} |\Psi_n\rangle + \text{c. c.}, \quad (11)$$

where $\phi_n(z, t) = k_n z - \omega_n t$, and the $|\Psi_n(x, y)\rangle$ are eigenmodes of the unperturbed (lossless and linear) waveguide problem:

$$(\mathbb{D}^{(\text{opt})} + ik_n \mathbb{P}^{(\text{opt})}) |\Psi_n\rangle = i\omega_n \mathbb{E}^{(\text{opt})} |\Psi_n\rangle. \quad (12)$$

The choice of expanding in terms of the eigenmodes of the unperturbed problem simplifies the formalism. In principle we could choose to expand in the eigenmodes of the full problem including the optical (and acoustic) loss, however this would require a full dual-space of eigenfunctions, greatly increasing the complexity of the derivation. For the relatively low-loss situations that occur in all Brillouin problems thus far this expansion should remain accurate. In the unperturbed case the modes are orthogonal with respect to the energy operator $\mathbb{E}^{(\text{opt})}$:

$$\langle \Psi_n | \mathbb{E}^{(\text{opt})} | \Psi_{n'} \rangle = \mathcal{E}_n \delta_{nn'}, \quad (13)$$

with the energy mode normalization factor

$$\mathcal{E}_n = \langle \Psi_n | \mathbb{E}^{(\text{opt})} | \Psi_n \rangle = \underbrace{\int dA \mathbf{E}_n^* \cdot (\epsilon^{(R)} \mathbf{E}_n) + \mathbf{H}_n^* \cdot (\mu \mathbf{H}_n)}_{\text{Energy of mode per unit length}}, \quad (14)$$

where the integral is evaluated over the entire x - y -plane. Likewise, we introduce the power flux of the mode:

$$\begin{aligned} \mathcal{P}_n = \langle \Psi_n | \mathbb{P}^{(\text{opt})} | \Psi_n \rangle &= \int dA (\mathbf{E}_n^* \cdot \mathbf{H}_n^*) \begin{pmatrix} \hat{\mathbf{z}} \times \mathbf{H}_n \\ -\hat{\mathbf{z}} \times \mathbf{E}_n \end{pmatrix} \\ &= 2\text{Re} \int dA \hat{\mathbf{z}} \cdot (\mathbf{E}_n \times \mathbf{H}_n^*), \end{aligned} \quad (15)$$

which can be regarded as the power normalization factor. This power flux may be used to introduce a second mode orthogonality relation that this time only applies to propagating modes:

$$\langle \Psi_n | \mathbb{P}^{(\text{opt})} | \Psi_{n'} \rangle = \mathcal{P}_n \delta_{nn'}. \quad (16)$$

Substituting into the system Eq. (10), the expansion Eq. (11) admits

$$\begin{aligned} \mathbb{E}^{(\text{opt})} \partial_t \left(\sum_n a_n e^{i\phi_n} |\Psi_n\rangle \right) + \mathbb{P}^{(\text{opt})} \partial_z \left(\sum_n a_n e^{i\phi_n} |\Psi_n\rangle \right) \\ + \mathbb{D}^{(\text{opt})} \left(\sum_n a_n e^{i\phi_n} |\Psi_n\rangle \right) + \text{c. c.} \\ = -\partial_t \left(\sum_n a_n e^{i\phi_n} \Delta \mathbb{E}^{(\text{opt})}(t) |\Psi_n\rangle \right) \\ - \mathbb{S}^{(\text{opt})} \left(\sum_n a_n e^{i\phi_n} |\Psi_n\rangle \right) + \text{c. c.} \end{aligned} \quad (17)$$

By using Eq. (12) and the product rule expressions

$$\partial_t (a_n e^{i\phi_n}) = e^{i\phi_n} (\partial_t a_n - i\omega_n a_n) = e^{i\phi_n} (\partial_t - i\omega_n) a_n, \quad (18a)$$

$$\partial_z (a_n e^{i\phi_n}) = e^{i\phi_n} (\partial_z a_n + ik_n a_n) = e^{i\phi_n} (\partial_z + ik_n) a_n, \quad (18b)$$

we can further simplify (17 to:

$$\begin{aligned} & \sum_n e^{i\phi_n} \left[\mathbb{E}^{(\text{opt})} \partial_t + \mathbb{P}^{(\text{opt})} \partial_z \right] a_n |\Psi_n\rangle + \text{c. c.} \\ &= - \sum_n e^{i\phi_n} \left[\mathbb{S}^{(\text{opt})} a_n + (\partial_t - i\omega_n)(a_n \Delta \mathbb{E}^{(\text{opt})}) \right] |\Psi_n\rangle + \text{c. c.} \end{aligned} \quad (19)$$

As a next step, we apply a rotating wave approximation (RWA), where we assume that amplitudes that oscillate with $\exp(i\omega t)$ evolve independently from those at $\exp(-i\omega t)$. This is generally a good approximation if the bandwidth of a physical process is small compared to the central frequency, i.e. if the time scale on which envelopes evolve is much larger than the oscillation period. This is clearly the case in Brillouin scattering, and manifests simply in dropping the complex conjugate terms:

$$\begin{aligned} & \sum_n e^{i\phi_n} \left[\mathbb{E}^{(\text{opt})} \partial_t + \mathbb{P}^{(\text{opt})} \partial_z \right] a_n |\Psi_n\rangle \\ &= - \sum_n e^{i\phi_n} \left[\mathbb{S}^{(\text{opt})} a_n + (\partial_t - i\omega_n)(a_n \Delta \mathbb{E}^{(\text{opt})}) \right] |\Psi_n\rangle. \end{aligned} \quad (20)$$

Next, we disentangle this single equation for many coupled optical amplitudes into a set of equations for one optical amplitude, each. This relies on the assumption that the optical modes $|\Psi_n\rangle$ form a complete orthogonal basis, which is why we chose the solutions to the lossless (Hermitian) problem Eq. (12) for our field expansion. We decouple the amplitudes by projecting Eq. (19) onto one specific mode:

$$\begin{aligned} & \langle \Psi_n | \sum_{n'} e^{i\phi_{n'}} \left[\mathbb{E}^{(\text{opt})} \partial_t + \mathbb{P}^{(\text{opt})} \partial_z \right] a_{n'} |\Psi_{n'}\rangle \\ &= - \langle \Psi_n | \sum_{n'} e^{i\phi_{n'}} \left[\mathbb{S}^{(\text{opt})} a_{n'} + (\partial_t - i\omega_{n'})(a_{n'} \Delta \mathbb{E}^{(\text{opt})}) \right] |\Psi_{n'}\rangle, \end{aligned} \quad (21)$$

and after dividing by the left hand phase factor and applying the orthogonality relations Eq. (13) and Eq. (16):

$$\begin{aligned} (\mathcal{E}_n \partial_t + \mathcal{P}_n \partial_z) a_n &= - \sum_{n'} e^{i\phi_{n'} - i\phi_n} \left[\langle \Psi_n | \mathbb{S}^{(\text{opt})} | \Psi_{n'} \rangle a_{n'} \right. \\ & \left. + \langle \Psi_n | (\partial_t - i\omega_{n'}) (a_{n'} \Delta \mathbb{E}^{(\text{opt})}) | \Psi_{n'} \rangle \right]. \end{aligned} \quad (22)$$

Next, we employ a slowly-varying envelope approximation, i.e. we assume that the physically relevant dynamic is described by envelope functions a_n that vary slowly compared to the time scale of their respective carrier frequencies and that quickly oscillating contributions average to zero. This slowly varying envelope approximation (SVEA) is intimately linked with the earlier RWA and they are often applied in conjunction. First, we discuss the term involving $\langle \Psi_n | \mathbb{S}^{(\text{opt})} | \Psi_{n'} \rangle$. For non-degenerate modes, the phase factor $e^{i\phi_{n'} - i\phi_n}$ oscillates quickly and the term can be dropped. For degenerate modes, this term can be non-zero and describe mode-conversion that is mediated by material loss. We will ignore this possibility and assume

$$\langle \Psi_n | \mathbb{S}^{(\text{opt})} | \Psi_{n'} \rangle = \mathcal{S}_n \delta_{nn'}, \quad (23)$$

with the damping constant \mathcal{S}_n , but we note that systems with strong loss might require the inclusion of such cross-coupling terms.

So far, we have arrived at a set of equations of the form

$$\begin{aligned} & (\mathcal{E}_n \partial_t + \mathcal{P}_n \partial_z + \mathcal{S}_n) a_n \\ &= - \sum_{n'} e^{i\phi_{n'} - i\phi_n} \langle \Psi_n | (\partial_t - i\omega_{n'}) (a_{n'} \Delta \mathbb{E}^{(\text{opt})}) | \Psi_{n'} \rangle. \end{aligned} \quad (24)$$

Now, we must make an assumption about the nature of $\Delta \mathbb{E}^{(\text{opt})}$. In Brillouin scattering, $\Delta \mathbb{E}^{(\text{opt})}$ describes the change of the waveguide due to an acoustic field $|\Phi(x, y, z, t)\rangle$, which we express in terms of an acoustic eigenmode according to Eq. (4b). Since we assume that $\Delta \mathbb{E}^{(\text{opt})}$ is proportional to the mechanical deformation and the deformation field is proportional to the real part of $|\Phi\rangle$, we make the ansatz

$$\Delta \mathbb{E}^{(\text{opt})}(x, y, z, t) = b(z, t) e^{iqz - i\Omega t} \Delta \mathbb{E}_\perp^{(\text{opt})}(x, y) + \text{c. c.}, \quad (25)$$

where the acoustic mode pattern is absorbed into the operator $\Delta \mathbb{E}_\perp^{(\text{opt})}(x, y)$. For the moment we are not too worried how exactly that works; we will revisit this point later. However, what we can say immediately is that $\partial_t(a_{n'} \Delta \mathbb{E}^{(\text{opt})})$ is small compared to $\omega_{n'} a_{n'} \Delta \mathbb{E}^{(\text{opt})}$, because both the envelopes $a_{n'}$ and b as well as the phase factor $e^{iqz - i\Omega t}$ are slow compared to the optical frequency $\omega_{n'}$. Within the SVEA, we can therefore simplify Eq. (24) as:

$$\begin{aligned} & (\mathcal{E}_n \partial_t + \mathcal{P}_n \partial_z + \mathcal{S}_n) a_n \\ &= i \sum_{n'} \omega_{n'} e^{i(\phi_{n'} - \phi_n)} \left[e^{i(qz - \Omega t)} \underbrace{\langle \Psi_n | \Delta \mathbb{E}_\perp^{(\text{opt})} | \Psi_{n'} \rangle}_{=Q_{nn'}} b + \text{c. c.} \right] a_{n'}, \end{aligned} \quad (26)$$

where we introduce the opto-mechanical perturbation overlap $Q_{nn'}$, which contains the interaction between the different optical states (which may be the same mode, or modes of different polarization), mediated by the operator $\Delta \mathbb{E}_\perp^{(\text{opt})}$ coming from the acoustic field. This form of the mode equation contains the constants \mathcal{E}_n and \mathcal{P}_n , which reflect well-defined physical constants of the optical mode, but whose values are arbitrary, because the modes can be normalized in any way. This can be resolved by dividing by either \mathcal{E}_n or \mathcal{P}_n . The latter is more in the spirit of classical (fibre-)optics Brillouin literature and leads to the form

$$\begin{aligned} & (v_n^{-1} \partial_t + \partial_z + \frac{1}{2} \alpha_n) a_n \\ &= \frac{1}{\mathcal{P}_n} i \sum_{n'} e^{i(\phi_{n'} - \phi_n)} \left[e^{i(qz - \Omega t)} \omega_{n'} Q_{nn'} b + \text{c. c.} \right] a_{n'}, \end{aligned} \quad (27)$$

where $v_n = \mathcal{P}_n / \mathcal{E}_n$ is the group velocity of the mode and α_n is the power loss parameter along the waveguide in units of m^{-1} . The factor 1/2 appears because the power damping parameter is twice the amplitude decay parameter that would naturally appear at this point, but is less commonly specified in the literature. Alternatively, one can divide by \mathcal{E}_n leading to

$$\begin{aligned} & (\partial_t + v_n \partial_z + \Gamma_n) a_n \\ &= \frac{1}{\mathcal{E}_n} i \sum_{n'} e^{i(\phi_{n'} - \phi_n)} \left[e^{i(qz - \Omega t)} \omega_{n'} Q_{nn'} b + \text{c. c.} \right] a_{n'}, \end{aligned} \quad (28)$$

with the amplitude damping parameter Γ_n in time (units s^{-1}). The latter approach is much more in line with the opto-mechanics literature, which typically does not involve propagating waves. In fact, if the modes are chosen to be normalized to $\mathcal{E}_n = \hbar \omega_n$ per unit length, then such a choice also permits us to link-up with quantum optics and the quantum cavity opto-mechanics literature. For this particular "quantum" normalization we find $\omega_{n'} Q_{nn'} / \mathcal{E}_n \approx Q_{nn'} / \hbar$ assuming $\omega_{n'} \approx \omega_n$.

In summary, the optical part of the problem is described by one such equation (Eq. (27) or Eq. (28)) per optical mode that participates in the Brillouin scattering process. Note that we have only assumed that both envelopes are slow compared to

the optical carrier. The further treatment depends on whether we assume that the envelopes a_n and b are also slow compared to the acoustic frequency Ω or not. Note also that one has to make identical assumptions for both the optical and the acoustic envelopes, because they are coupled to each other and different treatment would lead to significant errors. Therefore, we now derive the mode equation for the acoustic envelope and afterwards further restrict the system of equations to backward, forward, and intermodal Brillouin scattering.

B.2. Acoustic mode equation

The mechanical analogue to Maxwell's equations are the equations of linear elasticity, which comprise the relation between strain and mechanical displacement and the conservation of momentum:

$$\mathbf{S} = \nabla_s \mathbf{U}, \quad (29a)$$

$$\rho \partial_t^2 \mathbf{U} = \nabla \cdot \mathbf{T} + \mathbf{f}, \quad (29b)$$

where \mathbf{S} denotes the linear strain tensor, ∇_s the symmetric gradient operator, \mathbf{U} the infinitesimal mechanical displacement vector, ρ the mass density, \mathbf{T} the mechanical stress tensor (Cauchy stress), and \mathbf{f} the body force density. As in the electrodynamic case, the system needs to be closed by a constitutive relationship, which in the lossless case takes the form:

$$T_{ij} = \sum_{kl} c_{ijkl} S_{kl}, \quad \text{or equivalently} \quad S_{ij} = \sum_{kl} s_{ijkl} T_{kl}, \quad (30)$$

where we define the stiffness tensor c_{ijkl} and the compliance tensor s_{ijkl} [18]. Next, we introduce friction due to the dynamic viscosity tensor η_{ijkl} , which formally modifies the constitutive relation:

$$\tilde{T}_{ij} = \sum_{kl} (c_{ijkl} + \eta_{ijkl} \partial_t) S_{kl}. \quad (31)$$

However, by splitting the stress tensor into a lossless (Eq. (30)) and a dissipative part and then using the conservation of momentum equation, we can also express the effect of η_{ijkl} as a dissipative force density:

$$\mathbf{f}_i^{(\text{loss})} = -\nabla \cdot \boldsymbol{\eta} : (\nabla_s \mathbf{V}), \quad (32)$$

where $\mathbf{V} = \partial_t \mathbf{U}$ is the local velocity field. Furthermore, we introduced ':' as a shorthand notation for a double index contraction – for example Eq. (31) reads in this form $\tilde{\mathbf{T}} = (\mathbf{c} + \boldsymbol{\eta} \partial_t) : \mathbf{S}$. As in the optical case, we now introduce an acoustic state vector notation $|\phi\rangle = [\mathbf{T}, \mathbf{V}]^T$, where $\mathbf{T} = \mathbf{c} : \mathbf{S}$ is the lossless stress, i.e. $\mathbf{f}^{(\text{loss})} = \nabla \cdot (\mathbf{T} - \tilde{\mathbf{T}})$. With this, we can now write a compact master equation for the mechanical problem:

$$\mathbb{E}^{(\text{ac})} \partial_t |\phi\rangle + \mathbb{P}^{(\text{ac})} \partial_z |\phi\rangle + \mathbb{D}^{(\text{ac})} |\phi\rangle = -\mathbb{S}^{(\text{ac})} |\phi\rangle + |F\rangle \quad (33)$$

where $|F\rangle = [0, \mathbf{f}]^T$ is the external forcing term and the operators are defined as:

$$\mathbb{E}^{(\text{ac})} = \begin{pmatrix} \mathbf{s} : & 0 \\ 0 & \rho \end{pmatrix}, \quad \mathbb{P}^{(\text{ac})} = \begin{pmatrix} 0 & -\hat{z} \otimes_s \\ -\hat{z} \cdot & 0 \end{pmatrix}, \quad (34)$$

$$\mathbb{D}^{(\text{ac})} = \begin{pmatrix} 0 & -\nabla_{\perp, s} \\ -\nabla_{\perp} \cdot & 0 \end{pmatrix}, \quad \mathbb{S}^{(\text{ac})} = \begin{pmatrix} 0 & 0 \\ 0 & -\nabla \cdot \boldsymbol{\eta} : \nabla_s \end{pmatrix}.$$

Here, we define the symmetrized tensor product \otimes_s by $\hat{z} \otimes_s \mathbf{V} = (\hat{z} \otimes \mathbf{V} + \mathbf{V} \otimes \hat{z})/2$. As in the optical case, we now approximate

the acoustic state in terms of the eigenmodes of the unperturbed (lossless and no other external forcing) acoustic waveguide problem:

$$(\mathbb{D}^{(\text{ac})} + i\eta \mathbb{P}^{(\text{ac})}) |\Phi\rangle = i\Omega \mathbb{E}^{(\text{ac})} |\Phi\rangle, \quad (35)$$

where for the sake of simplicity, we will only include a single acoustic mode, leading to the aforementioned "expansion" Eq. (4b):

$$|\phi(x, y, z, t)\rangle = b(z, t) |\Phi(x, y)\rangle e^{iqz - i\Omega t} + \text{c. c.} \quad (36)$$

At first glance, this difference in the modal expansions for the optical and acoustic parts may appear unusual. However, it is justified by the fact that the nonlinear opto-mechanical processes that dominate Brillouin scattering (i.e. electrostriction/photoelasticity and radiation pressure and its related optical moving-boundary effect) constitute inelastic scattering processes between two photons and one phonon. As a result, these opto-mechanical nonlinearities can only mediate the transfer of energy and momentum between two optical modes via one acoustic mode, and not between two acoustic modes via one optical mode. Thus, opto-mechanically induced coupling between two acoustic modes requires them to be degenerate, in which case they will generally split into an opto-mechanically bright and a dark mode (see e.g. [34] for an example in cavity opto-mechanics). In such a case, the dark acoustic mode can be ignored and the Brillouin coupled mode equations should be formulated as described above in terms of the bright hybridized mode only. As a result the individual acoustic modes can be analyzed separately in most cases. A generalization to many acoustic modes is fairly straight-forward at the expense of additional subscript indices; an example can be found in [33].

We insert Eq. (36) into Eq. (33) and obtain in analogy to the optical mode equation:

$$(\mathcal{E}_b \partial_t + \mathcal{P}_b \partial_z + S_b) b = e^{-iqz + i\Omega t} \langle \Phi | F \rangle, \quad (37)$$

where we introduce the normalization constants

$$\mathcal{E}_b = \langle \Phi | \mathbb{E}^{(\text{ac})} | \Phi \rangle = \int dA \mathbf{T}^* : (\mathbf{s} : \mathbf{T}) + \mathbf{V}^* \cdot (\rho \mathbf{V}), \quad (38a)$$

$$\begin{aligned} \mathcal{P}_b &= \langle \Phi | \mathbb{P}^{(\text{ac})} | \Phi \rangle = - \int dA \hat{z} \cdot (\mathbf{T}^* \cdot \mathbf{V}) + \hat{z} \cdot (\mathbf{T} \cdot \mathbf{V}^*) \\ &= -2 \int dA \text{Re} \{ \hat{z} \cdot (\mathbf{T}^* \cdot \mathbf{V}) \}. \end{aligned} \quad (38b)$$

Next, we assume that the driving term $|F\rangle$ in Eq. (37) is due to optical forces, specifically, a result of optical intensity fluctuations. The optical intensity at a point (x, y, z) at time t is given by:

$$\begin{aligned} |E|^2(x, y, z, t) &= \left| \sum_n a_n(z, t) e^{i\phi_n} E_n(x, y) + a_n^*(z, t) e^{-i\phi_n} E_n^*(x, y) \right|^2 \\ &= \underbrace{\left[\sum_{nn'} e^{i(\phi_n + \phi_{n'})} a_n(z, t) a_{n'}(z, t) E_n(x, y) E_{n'}(x, y) + \text{c. c.} \right]}_{\text{co-rotating}} \\ &\quad + \underbrace{\left[\sum_{nn'} e^{i(\phi_n - \phi_{n'})} a_n(z, t) a_{n'}^*(z, t) E_n(x, y) E_{n'}^*(x, y) + \text{c. c.} \right]}_{\text{counter-rotating}}, \end{aligned} \quad (39)$$

where, as before, we use the short hand $\phi_n = ik_n z - i\omega_n t$. Among the two terms indicated by braces, the first ("co-rotating") one varies on the optical time scale, which is much

too fast for the mechanical system to react to and therefore effectively averages to zero. The only relevant term is the last one, denoted “counter-rotating”, because its time dependence is the result of two optical phases evolving in opposite directions. Therefore, it is reasonable to drop the first two terms in Eq. (39). Such an approximation, which replaces a full interaction term with only the counter-rotating ones is a rotating wave approximation (RWA), which we have encountered previously in the discussion of the optical field. The application of the RWA at this point is always appropriate, because the optical time scale is always many orders of magnitude faster than the acoustic scale.

Given that the optical forces are caused by intensity fluctuations, then within this RWA we may decompose $|F\rangle$ into the contributions that arise from the beat between each pair of optical modes:

$$|F(x, y, z, t)\rangle = \sum_{nn'} e^{i(\phi_n - \phi_{n'})} a_n(z, t) a_{n'}^*(z, t) |F_{nn'}(x, y)\rangle + e^{i(\phi_{n'} - \phi_n)} a_n^*(z, t) a_{n'}(z, t) |F_{n'n}(x, y)\rangle, \quad (40)$$

where we observe that the second term in the summand is the complex conjugate of the first term. Substituting this into Eq. (37) yields:

$$(\mathcal{E}_b \partial_t + \mathcal{P}_b \partial_z + S_b) b = e^{-i(qz - \Omega t)} \left[\sum_{nn'} e^{i(\phi_n - \phi_{n'})} a_n a_{n'}^* \langle \Phi | F_{nn'} \rangle + e^{i(\phi_{n'} - \phi_n)} a_n^* a_{n'} \langle \Phi | F_{n'n} \rangle \right]. \quad (41)$$

As with the optical equations, there are two obvious ways to normalize the equations: either with respect to the modal power \mathcal{P}_b :

$$(v_b^{-1} \partial_t + \partial_z + \frac{1}{2} \alpha_b) b = \frac{1}{\mathcal{P}_b} e^{-i(qz - \Omega t)} \left[\sum_{nn'} e^{i(\phi_n - \phi_{n'})} a_n a_{n'}^* \langle \Phi | F_{nn'} \rangle + e^{i(\phi_{n'} - \phi_n)} a_n^* a_{n'} \langle \Phi | F_{n'n} \rangle \right], \quad (42)$$

with the acoustic power loss parameter α_b in units of m^{-1} , or with respect to the modal energy \mathcal{E}_b :

$$(\partial_t + v_b \partial_z + \Gamma_b) b = \frac{1}{\mathcal{E}_b} e^{-i(qz - \Omega t)} \left[\sum_{nn'} e^{i(\phi_n - \phi_{n'})} a_n a_{n'}^* \langle \Phi | F_{nn'} \rangle + e^{i(\phi_{n'} - \phi_n)} a_n^* a_{n'} \langle \Phi | F_{n'n} \rangle \right], \quad (43)$$

with the acoustic amplitude decay parameter Γ_b in units of s^{-1} . As in the optical case, the energy normalization allows for easy connection to quantum theories by choosing $\mathcal{E}_b = \hbar \Omega$.

C. Coupled-mode equation parameters

We now present the explicit expressions for the parameters that appear in the coupled-mode equations (CMEs) derived thus far.

C.1. Damping coefficients

We start with the optical and acoustic damping parameters α_n and α_b (as spatial decay parameters) and Γ_n and Γ_b (as temporal decay parameters). It should be stressed that generally great care should be taken when taking damping coefficients from the literature as they may refer to the decay of either the energy or

the amplitude of a wave, the former being greater by a factor of two. Here, we have chosen to specify decay along the waveguide by the *power* decay coefficient α , because this is almost universally how waveguide loss is specified. In contrast, we opted to specify the decay with respect to time by the *amplitude* decay coefficient, because this is how Brillouin linewidths are usually specified in the literature.

We recall from Sec. B.1:

$$\alpha_n = \frac{2S_n}{\mathcal{P}_n} \quad \text{and} \quad \Gamma_n = \frac{S_n}{\mathcal{E}_n}, \quad (44a)$$

$$\text{where} \quad S_n = \langle \Psi_n | S^{(\text{opt})} | \Psi_n \rangle. \quad (44b)$$

As a side remark, we also find $\Gamma_n = v_n \alpha_n / 2$, i.e. the spatial decay parameter is a signed quantity, and the sign indicates in which direction the optical amplitude decays – preferably in the direction of propagation. With the definition of $S^{(\text{opt})}$, we find:

$$S_n = \int dA |\mathbf{E}(\mathbf{r})|^2 \sigma(\mathbf{r}). \quad (45)$$

where the integral extends over the entire transverse plane of the waveguide, but has nonzero contributions only inside the waveguide, of course. Likewise, we find for the acoustic decay parameters:

$$\alpha_b = \frac{2S_b}{\mathcal{P}_b} \quad \text{and} \quad \Gamma_b = \frac{S_b}{\mathcal{E}_b}, \quad (46a)$$

$$\text{where} \quad S_b = \langle \Phi | S^{(\text{ac})} | \Phi \rangle \quad (46b)$$

$$= \Omega^2 \int dA \sum_{ijkl} S_{ij}^*(\mathbf{r}) \eta_{ijkl}(\mathbf{r}) S_{kl}(\mathbf{r}). \quad (46c)$$

If Brillouin measurements are available for a given structure, these quantities can also be obtained from the measured Brillouin linewidth.

C.2. Opto-mechanical coupling coefficients

Next, we move on to the nonlinear coupling coefficients. From Eq. (26) we recall:

$$Q_{nn'} = \langle \Psi_n | \Delta \mathbf{E}_{\perp}^{(\text{opt})} | \Psi_{n'} \rangle, \quad (47)$$

where $\Delta \mathbf{E}_{\perp}^{(\text{opt})}$ denotes the change in the optical properties due to a mechanical deformation and the bra-ket is a stand-in for the correctly performed perturbation integral. We will not go into too much detail here, but it should be noted that the perturbation theory of deformation of dielectric interfaces is not a straight-forward application of the usual integrals known from e.g. quantum mechanics. Rather, some additional attention is required as to which electromagnetic fields are continuous across the interface. For further discussion of these issues, see [24, 35].

The optical coupling coefficient $Q_{nn'}$ has predominantly two contributions: from the change in the bulk permittivity of materials subjected to strain and from the displacement of dielectric interfaces. The former is known as the photo-elastic contribution $Q_{nn'}^{(\text{PE})}$, and the latter as the moving-boundary term $Q_{nn'}^{(\text{MB})}$. These two terms depend on which optical and acoustic modes specifically interact and they can differ in amplitude and phase so that they can even compensate each other for a specific mode combination [25]. The photo-elastic contribution is due to the mechanical strain linearly changing the permittivity (assuming a real-valued strain):

$$\Delta \varepsilon_{ij} = -\varepsilon_r^2 \sum_{kl} p_{ijkl} S_{kl}, \quad (48)$$

where all quantities in principle depend on the position vector and the proportionality factor p_{ijkl} takes the form of a fourth-rank tensorial material parameter known as the photo-elastic Pockels tensor. With this, the photo-elastic contribution can be evaluated:

$$Q_{nn'}^{(\text{PE})} = -\varepsilon_0 \varepsilon_r^2 \int dA \sum_{ijkl} [E_i^{(n)}(\mathbf{r})]^* E_j^{(n')}(\mathbf{r}) p_{ijkl}(\mathbf{r}) S_{kl}(\mathbf{r}), \quad (49)$$

where $E_i^{(n)}$ refers to the i -th electric vector component of the n -th optical mode. As for the moving-boundary terms, we only state the result and refer the reader to [24, 36] for more details:

$$Q_{nn'}^{(\text{MB})} = \int_{\mathcal{C}} d\mathbf{r} (\hat{\mathbf{n}} \cdot \mathbf{U}) \left[(\varepsilon_a - \varepsilon_b) \varepsilon_0 (\hat{\mathbf{n}} \times \mathbf{E}^{(n)})^* \cdot (\hat{\mathbf{n}} \times \mathbf{E}^{(n')}) - (\varepsilon_a^{-1} - \varepsilon_b^{-1}) \varepsilon_0^{-1} (\hat{\mathbf{n}} \cdot \mathbf{D}^{(n)})^* (\hat{\mathbf{n}} \cdot \mathbf{D}^{(n')}) \right], \quad (50)$$

where the integral runs over the contour \mathcal{C} that separates two dielectrics with permittivities ε_a and ε_b and the local interface normal vector $\hat{\mathbf{n}}$.

After examining the coupling coefficients that appear in the optical equations, we now turn towards the corresponding term in the acoustic equation, denoted $\langle \Phi | F_{nn'} \rangle$. This again can be decomposed into a bulk contribution and a surface term. Their physical origins are electrostriction and radiation pressure, respectively. Electrostriction is the mechanical strain that appears in any medium due to an electromagnetic intensity and is linear with respect to the intensity (assuming real-valued electric fields):

$$T_{ij} = -\varepsilon_r^2 \sum_{kl} E_i^{(n)} E_j^{(n')} p_{ijkl}, \quad (51)$$

where the material constant p_{ijkl} is the same Pockels tensor that also describes the photo-elastic effect. This is not a coincidence, because conservation of energy requires nonlinear processes to come in pairs as shown here. Depending on preference, this can be viewed as an example for either Maxwell relations in a description of the interaction as an isentropic process (see [23], p179) or as an example for Manley-Rowe relations in energy-conserving nonlinear optics ([1], p88). Likewise, the moving-boundary effect from Eq. (50) is partnered up with radiation pressure and generally, we can conclude that

$$\langle \Phi | F_{nn'} \rangle = i\Omega Q_{nn'}^*. \quad (52)$$

This holds under the assumption that the nonlinear interaction itself does not dissipate energy, but makes no assumption about the presence of linear loss. This is the case with the photo-elastic/electrostrictive effect and the moving boundary/radiation pressure effect. It does not hold for example for optical forces caused by the absorption of light, e.g. in the context of stimulated Rayleigh scattering or electrostriction-like “current-striction” in semiconductors [37]. Such systems require separate derivations for $Q_{nn'}$ and $\langle \Phi | F_{nn'} \rangle$.

D. Some common further approximations

In this subsection, we aim to simplify the model through further approximations. None of these approximations are “automatically” valid, one must always verify that they are appropriate for the problem at hand. Unless otherwise stated, they can be applied independently of each other.

D.1. Strict RWA, slowly varying envelopes and phase matching

In many cases, we can drop all terms in the interaction except those that are exactly phase-matched. To see when this occurs, we consider the energy-normalized equations Eq. (28) and Eq. (43):

$$(\partial_t + v_n \partial_z + \Gamma_n) a_n = \frac{i}{\mathcal{E}_n} \sum_{n'} e^{i(\phi_{n'} - \phi_n)} \quad (53a)$$

$$\times \left[e^{i(qz - \Omega t)} \omega_{n'} Q_{nn'} b + \text{c. c.} \right] a_{n'},$$

$$(\partial_t + v_b \partial_z + \Gamma_b) b = \frac{i}{\mathcal{E}_b} e^{-i(qz - \Omega t)} \quad (53b)$$

$$\times \left[\sum_{n'} e^{i(\phi_n - \phi_{n'})} \Omega Q_{nn'}^* a_n a_{n'}^* + \text{c. c.} \right].$$

These equations still describe the phase-matched interaction between optical and acoustic modes as well as the non-phase-matched contribution. One example for the latter is the static deformation of a waveguide due to the presence of light. Often, these effects are not of interest and are weak; the resonant excitation of acoustic waves is enhanced by the quality factor. However, this means that off-resonant effects can become relevant to the overall dynamics either when the acoustic Q-factor is very low or when the dynamic of a system is short compared to the acoustic time scale. The latter occurs for example in experiments using optical pulses below $\simeq 100$ ps.

We now assume a situation where resonant scattering is dominant and that all envelopes a_n and b vary slowly compared to the acoustic time scale Ω^{-1} . As a result, only driving terms that satisfy

$$\omega_n - \omega_{n'} \pm \Omega \approx 0, \quad (54)$$

will have an effect on the correct time scale. Conversely, all other terms can be dropped in a second rotating wave approximation. This RWA is more restrictive than the first RWA in Section B.1 in that it restricts the physics captured by the model to even fewer interaction terms.

A similar argument can be made about the spatial coordinate. By requiring that the envelopes vary slowly compared to the optical and acoustic wave lengths k_n^{-1} and q^{-1} , respectively, we can restrict the relevant interactions to those that satisfy

$$k_n - k_{n'} \pm q \approx 0. \quad (55)$$

This slowly varying envelope approximation (SVEA) and the RWA are generally applied together.

Finally, it is very common to combine Eq. (54) and Eq. (55) and to replace the “approximately equal” sign with an equals sign. As a result, the only interactions retained are those where the participating modes satisfy the phase matching conditions:

$$\omega_n - \omega_{n'} \pm \Omega = 0, \quad k_n - k_{n'} \pm q = 0. \quad (56)$$

It should be noted, however, that Eq. (55) and therefore also the phase matching conditions are linked to the assumption that all envelopes vary slowly compared to both k^{-1} and q^{-1} . As a result, it might not be strictly permissible to use phase matching in some instances of forward Brillouin scattering.

For all phase-matched interaction terms, i.e. those that satisfy Eq. (56), the phase factors such as $\exp(i(\phi_n - \phi_{n'}))$ and $\exp(iqz - i\Omega t)$ cancel with each other, so after neglecting non-phase-matched interaction terms, we obtain the simplified

CMEs:

$$(\partial_t + v_n \partial_z + \Gamma_n) a_n = \frac{i}{\mathcal{E}_n} \left[\sum_{n'}^{\omega_n - \omega_{n'} = \Omega} \omega_{n'} Q_{nn'} b a_{n'} + \sum_{n'}^{\omega_n - \omega_{n'} = -\Omega} \omega_{n'} Q_{nn'}^* b^* a_{n'} \right], \quad (57a)$$

$$(\partial_t + v_b \partial_z + \Gamma_b) b = \frac{i}{\mathcal{E}_b} \left[\sum_{nn'}^{\omega_n - \omega_{n'} = \Omega} \Omega Q_{nn'}^* a_n a_{n'}^* + \sum_{nn'}^{\omega_n - \omega_{n'} = -\Omega} \Omega Q_{nn'} a_n^* a_{n'} \right], \quad (57b)$$

where the summations cover only indices n' that satisfy the conditions $\omega_n - \omega_{n'} = \pm\Omega$, respectively.

D.2. Continuous Wave (CW) approximation

Some applications (such as Brillouin storage) require optical pulses, but a large class of experiments use (quasi-)CW optical fields. In such a setting all intensities $|a_n|^2$, $|b|^2$ should be constant in time (not in space), i.e. that the envelopes should have only a phase modulation, e.g. a harmonic phase $e^{-i\Delta\omega t}$. At least in the latter case we slightly adjust the carrier frequencies ω_n and Ω such that all envelopes a_n and b themselves become constant with respect to time. As a result, we can now simply drop the time derivatives in the coupled mode equations:

$$(v_n \partial_z + \Gamma_n) a_n = \frac{1}{\mathcal{E}_n} i \sum_{n'} e^{i(\phi_{n'} - \phi_n)} \left[e^{i(qz - \Omega t)} \omega_{n'} Q_{nn'} b + \text{c. c.} \right] a_{n'}, \quad (58a)$$

(one for each mode n)

$$(v_b \partial_z + \Gamma_b) b = \frac{i}{\mathcal{E}_b} e^{-i(qz - \Omega t)} \left[\sum_{nn'} e^{i(\phi_n - \phi_{n'})} \Omega Q_{nn'}^* a_n a_{n'}^* + \text{c. c.} \right]. \quad (58b)$$

However, this is only acceptable if the envelopes a_n and b really do not change in time, which means that the right hand sides of Eq. (58) must not depend on time, either. From this we see that this approximation is only appropriate if the coupling terms satisfy at least the frequency part of the phase matching condition:

$$\omega_n - \omega_{n'} \pm \Omega = 0. \quad (59)$$

Finally, it is convenient in CW problems to normalize amplitudes by power rather than energy. We find:

$$(\partial_z + \frac{1}{2}\alpha_n) a_n = \frac{i}{\mathcal{P}_n} \left[\sum_{n'}^{\omega_n - \omega_{n'} = \Omega} e^{i(k_{n'} - k_n + q)z} \omega_{n'} Q_{nn'} b a_{n'} + \sum_{n'}^{\omega_n - \omega_{n'} = -\Omega} e^{i(k_{n'} - k_n - q)z} \omega_{n'} Q_{nn'}^* b^* a_{n'} \right], \quad (60a)$$

$$(\partial_z + \frac{1}{2}\alpha_b) b = \frac{i}{\mathcal{P}_b} \left[\sum_{nn'}^{\omega_n - \omega_{n'} = \Omega} e^{i(k_n - k_{n'} - q)z} \Omega Q_{nn'}^* a_n a_{n'}^* + \sum_{nn'}^{\omega_n - \omega_{n'} = -\Omega} e^{i(k_{n'} - k_n - q)z} \Omega Q_{nn'} a_n^* a_{n'} \right]. \quad (60b)$$

The remaining phase factors of the form $e^{i(k_n - k_{n'} \pm q)z}$ can model detuning and cause complex interference effects along the waveguide if more than two optical modes are involved. Naturally,

they disappear as soon as proper phase matching is assumed. The great advantage of the CW approximation is that Eq. (60) is only a system of ordinary differential equations, which can be solved easily e.g. using standard Runge-Kutta integrators or in some cases even analytically.

D.3. Local acoustic response approximation

In many cases, the propagation length of the acoustic excitation is negligible compared to the other length scales of the problem, in particular the waveguide length and the conversion length. In this case, it is acceptable to assume $v_b = 0$. This is generally a very good approximation and may be used to simplify the development of PDE-solvers for the optical envelopes in transient problems (see Section 5). However, this assumption has great impact in conjunction with the stationary approximation, because it simplifies the equation for the acoustic envelope so far that it can be explicitly solved:

$$b = \frac{i\Omega}{\mathcal{E}_b \Gamma_b} \left[\sum_{nn'}^{\omega_n - \omega_{n'} = \Omega} e^{i(k_n - k_{n'} - q)z} Q_{nn'}^* a_n a_{n'}^* + \sum_{nn'}^{\omega_n - \omega_{n'} = -\Omega} e^{i(k_{n'} - k_n - q)z} Q_{nn'} a_n^* a_{n'} \right]. \quad (61)$$

This expression can now be substituted back into the optical mode Eq. (60a) to completely eliminate b .

E. Equations for backward Brillouin scattering: gain

We now restrict the equations derived thus far to the first important special case: backward stimulated Brillouin scattering (SBS) in a relatively long waveguide. Here “relatively long” means that the local acoustic response approximation discussed in Section D.3 can be applied. Furthermore, we assume that only one acoustic mode is relevant and we assume that the system is excited with a single CW mode. This allows us to apply the strict RWA presented in Section D.1.

From the dispersion diagram Fig. 4, we can see that a single acoustic wave can couple a single pump wave only into one Stokes and one anti-Stokes wave. Furthermore, we can see that they are not coupled by the same acoustic wave: The Stokes process uses an acoustic wave with phase velocity $c_p \approx \Omega/(2k)$, whereas the anti-Stokes process uses an acoustic wave with $c_p \approx -\Omega/(2k)$. Therefore, the two processes decouple and can be treated separately. We restrict ourselves to the Stokes process involving two optical amplitude fields: a_0 for the pump and a_1 for the Stokes. From the dispersion diagram and Eq. (56), we find for the acoustic wave:

$$q \approx 2k, \quad \Omega = \omega_0 - \omega_1. \quad (62)$$

From the symmetry of the optical band structure, we can furthermore conclude

$$v_1 = -v_0, \quad \Gamma_1 = \Gamma_0, \quad \alpha_1 = -\alpha_0. \quad (63)$$

Finally, the low number of modes in the problem suggests to drop the subscripts in the opto-mechanical coupling coefficient: $Q = Q_{0,1}$. As per our assumption, we use the continuous wave equations in the strict RWA [Eq. (60)]. Thanks to the small number of amplitudes, the baroque use of indices and summation

signs simplifies to:

$$(v_0^{-1}\partial_t + \partial_z + \frac{1}{2}\alpha_0)a_0 = -\frac{i\omega_0}{\mathcal{P}_0}Q^*a_1b, \quad (64a)$$

$$(v_1^{-1}\partial_t + \partial_z + \frac{1}{2}\alpha_1)a_1 = -\frac{i\omega_1}{\mathcal{P}_1}Qa_0b^*, \quad (64b)$$

$$(\partial_t + v_b\partial_z + \Gamma_b)b = -\frac{i\Omega}{\mathcal{E}_b}Qa_0a_1^*. \quad (64c)$$

Next, we assume that the optical fields remain approximately constant over the length scale of the acoustic decay ($\leq 100\mu\text{m}$ in most materials). This allows us to use Eq. (61), which in this case reads:

$$b \approx -\frac{i\Omega Q}{\mathcal{E}_b\Gamma_b}a_0a_1^*. \quad (65)$$

Upon substituting this back into Eq. (64), neglecting the time derivatives within a CW-approximation and by defining a new coupling parameter

$$g_0 = \frac{2\omega\Omega|Q|^2}{\mathcal{P}_0^2\mathcal{E}_b\Gamma_b}, \quad (66)$$

we end up with the well-known coupled-mode equations for backward SBS:

$$(\partial_z + \frac{1}{2}\alpha_0)a_0 = -\frac{1}{2}g_0\mathcal{P}_0|a_1|^2a_0, \quad (67a)$$

$$(\partial_z + \frac{1}{2}\alpha_1)a_1 = \frac{1}{2}g_0\mathcal{P}_0|a_0|^2a_1. \quad (67b)$$

The parameter g_0 is the power gain coefficient, measured in units of $\text{m}^{-1}\text{W}^{-1}$. It is furthermore possible to neglect the phase information carried in the complex amplitudes by introducing optical power amplitudes $\pi_n = \mathcal{P}_n|a_n|^2$ leading to the coupled mode power equations:

$$(\partial_z + \alpha_0)\pi_0 = -g_0\pi_0\pi_1, \quad (68a)$$

$$(\partial_z - \alpha_0)\pi_1 = g_0\pi_0\pi_1, \quad (68b)$$

whose most important subtlety is that the factors 1/2 in front of the decay and gain coefficients vanish. This pair of equations can be solved analytically.

F. Equations for forward Brillouin scattering: phase modulation

Finally, we consider the modal equations for a typical forward Brillouin situation in a long waveguide such as a structured fibre. Forward Brillouin scattering differs significantly from backward SBS in that multiple optical frequency lines participate in the interaction, with one acoustic mode mediating the coupling between them [33]. As before, we assume that only one acoustic mode is relevant, which this time we assume to be thermally excited rather than stimulated by an optical pump. Again, we will employ the local acoustic response approximation, but this time we will forgo the strict RWA.

From the dispersion diagram in Fig. 5, we can see that a single acoustic wave does not merely couple a pump to the Stokes. Instead, a single acoustic wave couples each optical pump or (anti-)Stokes line to its immediately neighbouring lines, potentially leading to cascaded scattering. In order to fully capture this, we keep the weak rotating wave approximation and assume a single optical mode that is modulated at multiples of the acoustic frequency Ω . Furthermore, we note in the dispersion diagram that forward scattering involves acoustic modes that

are intersected by the light line of the optical mode index and therefore must be higher order modes very close to cut-off:

$$q \ll k, \quad \Omega = c_p q. \quad (69)$$

As a result, we can ignore acoustic propagation altogether.

We start the description of the problem by restating Eq. (27) for a single optical amplitude a_0 :

$$(v_0^{-1}\partial_t + \partial_z + \frac{1}{2}\alpha_0)a_0 = \frac{i\omega}{\mathcal{P}_0} \left[\underbrace{Q^*\tilde{b}}_{\text{AS. P.}} + \underbrace{Q\tilde{b}^*}_{\text{S. P.}} \right] a_0, \quad (70)$$

where v_0 , α_0 and \mathcal{P}_0 are the group velocity, amplitude damping coefficient and normalization power of the optical mode, and \tilde{b} is a phase transformation of the acoustic amplitude b introduced in order to simplify the notation:

$$\tilde{b} = \exp[i(qz - \Omega t)]b. \quad (71)$$

The optical source terms are annotated according to their physical role: the term ‘‘S. P.’’ describes the Stokes process, while the term ‘‘AS. P.’’ describes the anti-Stokes process.

A key feature of Eq. (70) is that the source term on the right hand side is purely imaginary and therefore only a pure phase modulation, but leaves the optical intensity $|a_0|^2$ unchanged. This is significant, because when we restrict Eq. (43) to the given problem, we find that the acoustic field is driven only by the optical intensity:

$$(\partial_t + \Gamma_b + i\Omega)\tilde{b} = -\frac{i\Omega(Q + Q^*)}{\mathcal{E}_b}|a_0|^2, \quad (72)$$

where we have set the acoustic group velocity to zero.

The effect is that in the absence of optical loss, the optical forces and therefore the acoustic intensity do not change along the waveguide. The optical and the acoustic mode equations are effectively decoupled and can be solved separately. For the acoustic problem this is straight-forward by integration in time. Solving the optical problem is slightly trickier and best done by integrating along the characteristic of the optical advection problem. To this end, we assume that an optical field is injected into the waveguide at $z = 0$ with a time-dependent signal given by $A(t)$. In the case of vanishing optical loss $\alpha_0 = 0$, we can obtain a closed expression:

$$a_0(z, t) = A\left(t - \frac{z}{v_0}\right) \exp\left[-ig_0\Gamma_b\mathcal{P}_0z\right. \\ \left. \times \int_0^\infty dt' \left|A\left(t - t' - \frac{z}{v_0}\right)\right|^2 e^{-\Gamma_b t'} \sin(\Omega t')\right]. \quad (73)$$

The opto-mechanical coupling strength is hidden in the parameter g_0 , which has the same form as the power gain parameter from backward SBS:

$$g_0 = \frac{2\omega\Omega|Q|^2}{\mathcal{P}_0^2\mathcal{E}_b\Gamma_b}, \quad (74)$$

but now describes a phase modulation rather than an amplification effect. For forward Brillouin scattering there is a characteristic length associated with this phase modulation, which determines when higher Stokes orders will appear. From Eq. (74) this length is

$$L_c = \left[g_0\mathcal{P}_0|A(0)|^2\right]^{-1} = \frac{1}{g_0P_{\text{pump}}}, \quad (75)$$

where P_{pump} is the input power of the pump.

It should be stressed that the discussion so far applies to optical waveguides without dispersion. This is significant, because any form of dispersion (or more generally: ω -dependent optical properties such as resonances in a Sagnac-loop) will change the relative phases between Stokes and corresponding anti-Stokes and thereby translate the pure phase modulation of the forward opto-mechanical interaction to a partial amplitude modulation. This means that the addition of dispersive elements of any kind can be used to turn forward Brillouin scattering into a gain mechanism (or an “anti-gain” mechanical cooling mechanism for opposite dispersion). This is one of the regimes where Brillouin scattering dynamics and cavity opto-mechanics cross over into each other, as indicated by the appearance of concepts such as mechanical cooling.

4. MATERIALS AND PLATFORMS

We see from Section 3 that Brillouin interactions are determined by a broad selection of tensors for the waveguide material, including the permittivity, stiffness, mass density, phonon viscosity, and photoelastic tensors. In addition under certain circumstances we may also need to know other material tensors, such as the third-order stiffness tensor [47]. Designing a Brillouin platform therefore presents a considerable challenge in complexity, in which all material parameters can play an important role. In this section we discuss how the material coefficients in general affect the strength of Brillouin scattering, and outline the main factors determining the choice of materials for Brillouin waveguide experiments.

In general the strength of the Brillouin interaction depends on three things: a strong innate coupling strength of the interaction (as provided by the high values of the components of the Pockel’s tensor, or by strong radiation pressure contributions), low loss of both optical and acoustic fields, and good confinement of both optical and acoustic modes (with a good overlap between them). Of these requirements, acoustic confinement is often the key challenge, especially for backward Brillouin devices which rely on TIR for confinement. This is because material combinations that have been designed as optical waveguides are often very poor acoustic waveguides. The underlying reason for this is that a high refractive index is generally correlated with high stiffness for many materials - silicon and diamond have among the highest refractive indices and stiffnesses, whereas polymers have low stiffness and moderate index. A high stiffness will in turn correspond to a high acoustic velocity. A high-index, stiff waveguide core on a low-index, relatively soft substrate — such as a silicon-on-silica nanowire — will therefore confine the optical field, but the acoustic field will be slower in the cladding than in the core and so will leak away too rapidly for Brillouin effects to be measured.

There are several approaches to overcoming the challenge of confinement. The first approach is to isolate the waveguide in air — this approach is the standard in any case for forward Brillouin scattering. In principle this should work for any material, and the main difficulty of this approach is one of fabricating sufficiently long, sufficiently stable suspended waveguides. Another approach to the confinement problem is to look for more appropriate materials. The doping of Silica fibre with germanium so as to create an optical waveguide fortuitously lowers the acoustic wave-speed in the core [17], and this means that standard single-mode fibre is a guide for both acoustic and optical modes. There also exists a class of materials that have both high refractive indices and that are mechanically soft: these are

the soft glasses, and in particular chalcogenide glasses [48]. An As_2S_3 waveguide core on a silica substrate will confine both acoustic and optical modes, and in addition has strong Pockel’s coefficients. Additional approaches to solving the confinement problem have also been suggested, including the use of metamaterials, photonic crystals, and phononic crystals [29, 49].

An “ideal” waveguide for Brillouin scattering is therefore made from one or more materials that possess high refractive indices (ensuring optical confinement), which are elastically soft (ensuring acoustic confinement), and possesses large photoelastic coefficients (ensuring strong photoelastic interactions), as well as low viscoelastic coefficients (ensuring low acoustic loss). If radiation pressure contributes strongly to the Brillouin coupling, the material and platform would also be chosen to yield radiation pressure contributions that add constructively to the electrostrictive contributions. Frequently there is a trade-off between all of these requirements, and no material is “ideal”.

A major problem in contemporary Brillouin scattering research is a scarcity of complete materials information in the literature. In particular, results for the phonon viscosity tensor are incredibly challenging to find, but may in certain instances be entirely deduced from experimental measurements of optical linewidths or quality factors [39]. Two useful repositories of physical properties constants include the CRC Handbook (which possesses for example tables of elastic constants [44]) and the Springer Materials database (for example, on tables of high-frequency optical properties [50]). With this scarcity in mind, we present a collection of material coefficients in Table 1 for a range of commonly-used materials present in photonic waveguides, assembled from a wide range of published works. However, we emphasise that this table does not even begin to describe the diversity of solid, liquid, and gaseous media that have been studied in the Brillouin literature across a range of pump frequencies. Examples of the actual Brillouin gains and coupling strengths for these materials in specific waveguide geometries are computed in the Appendix. In addition to the tensors listed in Table 1, it is important to keep in mind that other intrinsic material properties and wave effects may play a role in realising the Brillouin scattering gains/couplings calculated in this tutorial. As mentioned earlier, our treatment omits the presence of all optical losses but does incorporate linear elastic losses (as viscoelastic effects ultimately determine optical linewidths). In certain circumstances, the presence of linear and nonlinear optical losses may need to be considered (i.e., where two- and three-photon absorption effects [51] and free carrier absorption [52] are important). In materials such as Si and GaAs, these losses can be significant and subsequently pose a challenge in realising theoretically estimated results [53]. This gives soft glasses a considerable advantage over semiconductor materials such as Si and GaAs. That said, these glasses often have drawbacks of their own, in that effects such as photodarkening and crystallisation can prove a challenge in the fabrication of such structures [54].

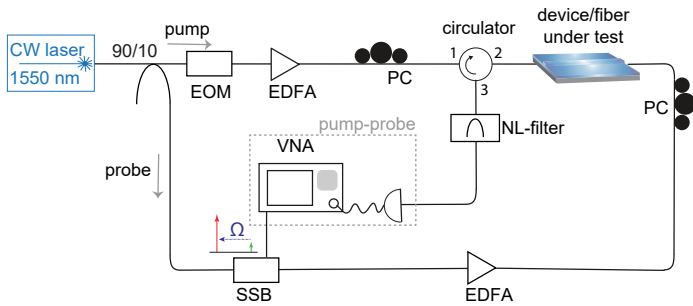
5. BRILLOUIN MEASUREMENTS

We now consider, in detail, several examples of important Brillouin experiments. This list is not intended to be exhaustive, but is intended to provide a reasonable starting point for setting up experiments and performing basic modelling to check the results. In each case we discuss the experimental setup, relate this to the equations in Section 3, and give examples of the type of output that one can expect.

Table 1. Optical, elastic, viscoelastic, and photoelastic bulk parameters for technologically relevant materials at pump wavelength of 1550 nm: relative permittivity ϵ_r ; stiffness tensor coefficients C_{ij} (units of [GPa]) and material density ρ (units of [$\text{kg} \cdot \text{m}^{-3}$]); phonon viscosity coefficients η_{ij} (units of [$\text{mPa} \cdot \text{s}$]); and photoelastic tensor coefficients p_{ij} where subscripts are in Voigt form.

Material	ϵ_r	Ref.	C_{11}	C_{12}	C_{44}	ρ	Ref.	η_{11}	η_{12}	η_{44}	Ref.	p_{11}	p_{12}	p_{44}	Ref.
SiO ₂ (fused)	2.1025	[38]	78.5	16.1	31.2	2200	[18]	1.6	1.29	0.16	[39]	0.121	0.271	-0.075	[40]
As ₂ S ₃	6.0025	[41]	18.9	6	6.4	3200	[42]	1.8	1.45	0.18	[39]	0.25	0.24	0.005	[42]
Si [100]	12.0805	[43]	165.8	63.9	79.6	2331	[44]	5.9	5.16	0.62	[45]	-0.094	0.017	-0.051	[40]
GaAs [100]	11.3582	[46]	118.8	53.7	59.4	5317	[44]	7.49	6.57	0.72	[45]	-0.165	-0.14	-0.072	[44]

a) Pump-probe setup



b) Setup for noise-initiated backward SBS

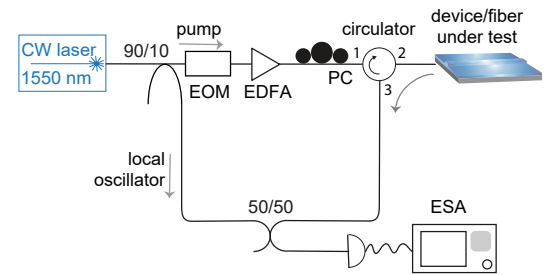


Fig. 7. Experimental setups for backward Brillouin scattering. a) Measurement of backward Brillouin scattering arising from an optical probe. b) Measurement of backward Brillouin scattering initiated from noise with a CW pump laser. This setup is based on heterodyne detection. The backscattered light interferes with a local oscillator (from the original laser) and the result can be observed at the electrical spectrum analyzer (ESA). Components in both setups: EDFA, erbium-doped fiber amplifier; PC, polarization controller; VNA, network analyzer; SSB, single-sideband modulator; EOM, electro-optic modulator; NL-filter, narrow-linewidth filter.

A. Pump-probe measurement of backward Brillouin scattering

The fundamental configuration of backward Brillouin scattering is the pump-probe setup, shown in Fig. 7. In this setup a narrow-linewidth laser is used as a pump from which the probe is carved off, and is then downshifted by an amount equal to the Brillouin frequency shift. The two beams are injected from opposite sides into the waveguide and interfere within it. The pump-probe experiment gives a highly-accurate measurement of the Brillouin response and is usually used to determine the Brillouin spectrum, including the linewidth and gain of a waveguide.

The basic setup for pump-probe detection is shown in Fig. 7a. A narrow-linewidth laser (e.g. external cavity laser) is separated using a fibre coupler or beam splitter into two arms: the stronger (typically 90%) being the pump and the weaker forming the probe arm. The probe arm is down-shifted in frequency using a modulator — for this purpose an RF-controlled electro-optic modulator (EOM) can be used; a single-sideband modulator can be employed to eliminate the higher-frequency sideband. The used RF-source can either be an independent RF-generator or the output channel of a network analyzer (Fig. 7a). Both pump and probe are amplified by an Erbium-doped fiber amplifier (EDFA), but the pump is typically about 10 times higher in power than the probe. A trick to increase the optical pump power in the device under test while keeping the average power low is to implement long pulses (about 50 ns) on the CW light by using an EOM before the EDFA. The pump and probe are launched from oppo-

site sides into the optical waveguide or fiber under test. While propagating through the waveguide, the probe will be amplified by backward Brillouin scattering, depending on the frequency difference between the pump and the probe. The backward-propagating light (amplified probe) is collected by means of a circulator, which allows the pump entering the waveguide in one direction and separating the counter-propagating probe light. At the output of the circulator, the backward-propagating light is detected by a photodiode, which is connected to the input of the network analyzer. In order to remove backscattered light stemming from Rayleigh scattering or reflection from the facets, a narrow bandwidth filter (e.g. 3 GHz) should be used on the probe light. As all Brillouin processes are polarization-dependent, the polarization of the pump and probe light has to be controlled and aligned in the waveguide or fiber under test. By sweeping the frequency of the probe and detecting the corresponding amplification on the network analyzer, the Brillouin gain spectrum is then recorded. A typical measurement of a pump-probe setup is shown in Fig. 11a). This represents the Brillouin gain spectrum with a maximum at the Brillouin frequency shift of 7.58 GHz and a linewidth of about 30 MHz (values for a chalcogenide As₂S₃ waveguide). When increasing the pump power level further, we can enter the regime of pump depletion, which can be observed in the spectrum as a flattening of the gain curve and finally a dip in the center of the gain spectrum. In the inset of Fig. 11a), the linewidth of the Brillouin spectrum with increasing input pump power is depicted, from which we can observe the typical narrowing of the Brillouin spectrum.

To model the evolution of the fields in backward Brillouin scattering, we employ the coupled mode equations (64), which can be solved numerically with one of several available methods for solving coupled partial differential equations [55]. The simplest approach is to employ a transformation of coordinates $\zeta_j = x - v_j t$ for each field to a reference frame that is co-propagating with the j^{th} envelope's velocity v_j . This characteristic transformation converts the system of partial differential equations Eq. (64) to a coupled system of ordinary differential equations, which can then be solved using a Runge-Kutta, or even an Euler, method algorithm that iterates in time. Because of the different scales of the pulse velocities, it is difficult to obtain better than linear convergence using this method, however it has the advantage of being extremely simple to implement. Fig. 8 shows the computed magnitude of the acoustic and optical field evolution along the waveguide for series of pulsed pump and Stokes beams, as well as the solution in steady state. In solving these equations we assume that the optical field is well represented by the mode which best fits the launch condition of the light into the waveguide (for example, the fundamental mode with TE polarization); the procedure for computing the coupling coefficients for this mode from the material and waveguide properties is given in the Appendix.

B. Measurement of noise-initiated backward Brillouin scattering

Noise-initiated Brillouin scattering can be thought of as the fundamental Brillouin response of the waveguide. It is often the first type of measurement that is performed when a new Brillouin-active waveguide is fabricated, in order to determine the approximate location of the Brillouin shift for future pump-probe measurements. Note that for short samples (e.g. silicon-based waveguides) the noise-initiated backward measurement might not be suitable due to the limited interaction length and possible high optical losses.

The measurement setup for noise-initiated backward Brillouin scattering (e.g. [56]) uses heterodyne detection and is depicted in Fig. 7b. The power of a narrow-linewidth laser (e.g. external cavity laser) is split into two parts: a strong pump and a weaker local oscillator. The pump is amplified by an EDFA, controlled in polarization and launched into a circulator to separate both optical propagation directions. Also here an EOM carving long pulses into the CW light can be used before the EDFA, in order to increase the peak pump power. The amplified pump then enters the fiber or the waveguide under test. The pump is backscattered due to longitudinal acoustic waves. This process is initiated by thermal phonons that follow the Bose-Einstein distribution, depending on their frequency and the environment's temperature. The backscattered optical waves pass again through the circulator and its output interferes via a coupler with the local oscillator stemming from the original laser. The interfered light is then detected by an amplified photodetector that enables the detection of low-power signals. A radiofrequency DC-block (high-pass filter) is used to block the backscattered light that stems from Rayleigh scattering and facet reflections and therefore arises at the same frequency as the local oscillator. The photodetector is connected to an electrical spectrum analyzer with a bandwidth that is greater than the Brillouin frequency shift. The lower the electronic noise level, the easier the detection.

A typical measurement of the noise-initiated Brillouin spectrum is shown in Fig. 11b) for different input pump power levels.

This measurement has been taken in a photonic crystal fiber made out of silica. The Brillouin frequency shift is at 11.09 GHz. In the low power regime the measurement of the spectrum has a low signal-to-noise ratio. When increasing the optical power, a smooth Lorentzian curve similar to the one in a pump-probe measurement can be obtained. Also here, a narrowing of the Brillouin linewidth with increasing input power can be observed.

The modelling of noise-initiated Brillouin scattering is less often needed, since the main purpose is usually to measure the overall Brillouin character of the device under test. To model this we modify the coupled-mode equations (64) by adding a small random part to the acoustic field $b(z, t)$, resulting in the dynamic equation [57]

$$(\partial_t + v_b \partial_z + \Gamma_b) b = - \frac{i\Omega}{\mathcal{E}_b} Q^* a_0 a_1^* + \sqrt{\sigma_b} R(z, t). \quad (76)$$

Here, the function $R(z, t)$ is a complex-valued white noise term (Langevin noise), with zero mean and auto-correlation given by $\langle R(z, t) R^*(z', t') \rangle = \delta(z - z') \delta(t - t')$. The strength of the noise is given by

$$\sigma_b = \frac{2k_B T \Gamma_b}{\mathcal{E}_b}, \quad (77)$$

where T is the temperature of the waveguide core, k_B is Boltzmann's constant. As in the noiseless pump-probe case, these equations can be solved numerically by transforming the spatial coordinates of each field to a reference frame that co-propagates with the mode velocity; the stochastic term can then be integrated using an Euler-Mayurama step [57].

C. Pump-probe measurement of forward Brillouin scattering

Forward Brillouin scattering is inherently different from backward Brillouin scattering because the phase matching condition is greatly relaxed (see Fig. 5). The acoustic modes that are involved in forward Brillouin scattering are nearly-standing waves that are confined by the transverse section of the waveguide, and so are almost independent of the optical frequency — this can be seen from the acoustic band in Fig. 5a, which is almost flat for small wave numbers. This means that every optical wavelength can couple to the same acoustic mode. This has far-reaching consequences for the measurement of forward Brillouin scattering. First of all, to excite the transverse acoustic modes, an optical pump can be used that is spectrally distant from the probe wave, where the forward Brillouin scattering is observed. Secondly, the transverse acoustic modes modulate the phase and polarization of the probe wave, and so the best way to measure forward Brillouin scattering is using an interferometric setup.

C.1. Direct pump-probe setup

This experimental configuration follows the pattern of the pump-probe measurement of backward Brillouin scattering, and is shown in Fig. 9a). A powerful pump is launched into a fiber, exciting the transversely-confined acoustic modes in the fiber. The pump is intensity modulated to form strong optical pulses via an electro-optic modulator. Due to the relaxed phase matching condition, a probe laser can experience the phase modulation induced by the excited acoustic modes [28]. The frequency sidebands of the probe wave that are created due to the phase modulation can then be detected spectrally, most conveniently by interference with a local oscillator. One advantage of this experimental scheme is that the polarization of pump and probe can easily be controlled with respect to each other. This setup can also be combined with a fiber loop, as has been implemented

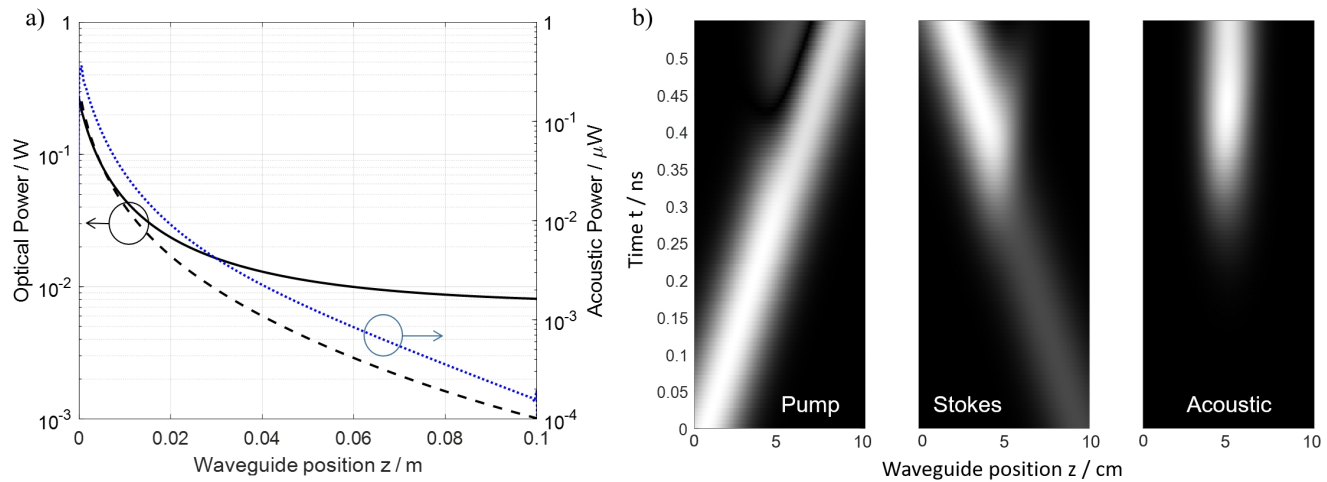


Fig. 8. a) Plot of pump (solid black line), Stokes (dashed black) and acoustic (dotted blue) powers in backward Brillouin scattering, for continuous pump and Stokes fields input from left and the right respectively. Note that although the Stokes field appears to “decay” it is propagating from right to left and so is gaining in power. These calculations are performed for the fundamental TE mode of a 10 cm-long rectangular silicon waveguide (200nm x 450nm) suspended in air; at an optical wavelength of 1550 nm the acoustic frequency is 17.31 GHz with linewidth of 14.39 MHz, resulting in a backward SBS gain of $2188 \text{ W}^{-1} \text{ m}^{-1}$. The input pump power is 0.3 W at the beginning of the waveguide ($z = 0$), with input Stokes power of 1 mW at the end of the waveguide ($z = 0.1$ m). b) Pump, Stokes and Acoustic powers for pump and Stokes pulses. Both Stokes and acoustic waves grow when the two pulses interact at the middle of the waveguide (5cm) at around $t = 0.25$ ns, at the expense of the pump.

in Ref. [58] in order to gain sensitivity. We note here that pulses, rather than a modulated continuous wave, can also be used to directly measure forward Brillouin scattering, which is known to cause temporal shifts between successive solitons propagating in optical fibres [59].

C.2. Dual pump setup

This setup [58] uses two optical pumps that are separated by the acoustic frequency (Fig. 9b). Both optical pumps are amplified and launched into the fiber or waveguide under test. While they are propagating through the waveguide, there is an energy transfer between them, mediated by the transverse acoustic mode. While the amplitude of both pumps is the same at the entrance of the fiber, there will be a difference in amplitude at the output of the fiber. By sweeping the frequency difference between the two optical pumps, the acoustic resonance spectrum can be observed by detecting both optical frequencies with an interferometer or an optical spectrum analyzer. The difference of this setup to the previous one is that the energy transfer between two co-propagating optical waves is detected directly, rather than having the probe at a remote frequency modulated by excited acoustic phonons stemming from the interaction with the pump.

The dynamics of forward Brillouin scattering are described by the coupled mode equations Eq. (70) and Eq. (72). These can either be integrated analytically (see discussion in Sec. 3.F), or can also be integrated numerically using the same approach as in backward Brillouin scattering (see Sec. 5.B). The amplitudes of two interacting beams undergoing forward Brillouin scattering are shown in Fig. 10. At the beginning of the waveguide the Stokes (and anti-Stokes) signals grow linearly as the pump depletes quadratically, giving the appearance of “gain” in the Stokes. However as the evolution continues the first-order Stokes combine with the pump to form higher-order Stokes and anti-Stokes lines. The amplitude of the acoustic mode remains

constant, since the Stokes process, which creates phonons, is perfectly balanced by the anti-Stokes process, which annihilates them. The acoustic field therefore plays the role of a constant-strength phase modulator of the optical signal.

D. Measurement of noise-initiated forward Brillouin scattering

Because the primary characteristic of forward Brillouin scattering is that it induces phase modulation, the noise-initiated forward process is readily measured using an interferometric setup. A commonly used interferometer is a Sagnac loop [60, 61] where 50% of the light travels through a pathway and the other 50% propagates through the same pathway but in opposite direction (Fig. 9c). This setup can detect both radial and torso-radial acoustic modes. The simplified setup is depicted in Fig. 9c. An amplified laser is controlled in polarization and enters a 50/50 fiber optical coupler. The two outputs of the coupler are connected to the fiber under test. The polarization is controlled before entering the coupler and inside the fiber loop. As both optical waves travel through the same optical path in a counterpropagative way, the polarization can be adjusted such that there is destructive interference at output B and constructive interference at output A (Fig. 9c). The tuning of the interference condition is possible due to the residual birefringence of the fiber loop and other components, inducing a polarization dependent phase shift. However, each optical path accumulates the phase modulation due to transverse acoustic modes in the fiber or waveguide. As these acoustic modes are incoherent, both optical paths do not accumulate the same phase modulation. This leads to a significant signal at output B because both optical paths are no longer equivalent. The signal can then be detected with an amplified photodiode and observed with an RF spectrum analyzer. Note that a major advantage of this setup is that all transverse acoustic modes can be measured at the same time, in contrast to CW pump-probe measurements where prior knowledge of the frequency of the acoustic modes is essential [62, 63].

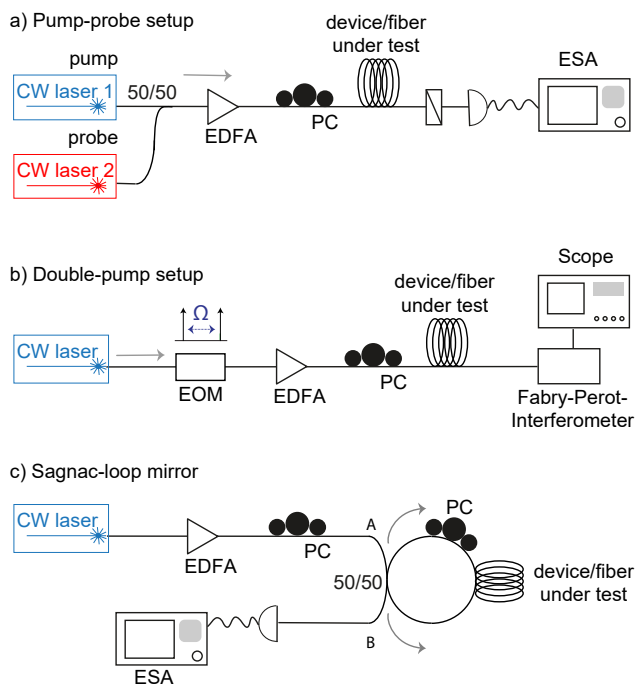


Fig. 9. Experimental setups for forward Brillouin scattering. a) In the pump-probe setup, both optical waves are co-propagating and the frequency difference of pump and probe can be freely chosen (taking into account the dispersion). The measurement can be taken at the ESA or oscilloscope. b) The double-pump setup is a specific pump-probe setup where energy is transferred from one sideband to the other sideband of an EOM when the frequency difference of the sidebands matches the acoustic frequency. The result can be measured by a Fabry-Perot-Interferometer. c) The Sagnac-loop mirror is an interferometric setup and response of the transverse acoustic modes is observed at the ESA. Components in the setups: EDFA, erbium-doped fiber amplifier; PC, polarization controller; EOM, electro-optic modulator.

The Sagnac loop - or Sagnac mirror - not only provides an interferometric measurement solution but also helps to remove a large portion of the amplified laser light, which would destroy a sensitive photodiode. At the same time, a sensitive photodiode must be used because the signature of the phase modulation is very weak. An example of such measurement is shown in Fig. 11c), where the plethora of acoustic modes in a standard single mode silica fiber (25 m) can be observed.

E. Applications of backward Brillouin scattering: distributed sensing setup and optical memory

All measurement techniques discussed thus far measure the Brillouin response integrated over the whole length of the fiber or over the entire waveguide on a chip. This means that possible changes in the Brillouin spectrum due to structural inhomogeneities of the waveguide or other parameters that change the Brillouin response such as the temperature or strain will lead to a broadening of the spectrum [47]. To resolve the local response of backward Brillouin scattering one can find several methods in the Brillouin sensing community. Some in-depth reviews and tutorials can be found in [9, 64, 65]. Here, we only give a short

overview. The original idea of a distributed measurement of backward Brillouin scattering uses a pulsed pump (intensity pulse) and a CW probe wave, which are separated by about the Brillouin frequency shift [10]. This setup corresponds to the experimental setup in Fig. 12 including an intensity modulator to create pump intensity pulses (Module 1). While the pump pulse travels through the waveguide, the CW probe is amplified, and this can be measured on an oscilloscope. Depending on the exact value of the Brillouin frequency shift at each position in the waveguide, the amplification is higher or lower. By sweeping the frequency difference between pump and probe, the Brillouin spectrum can be resolved along the fiber or waveguide. This technique is called Brillouin optical time domain analysis (BOTDA) and the main drawback is the limited spatial resolution of 1 m, which arises due to the limited acoustic lifetime of 10 ns in silica. To increase the spatial resolution several other techniques have been proposed, such as using phase pulses instead of intensity pulses in the Brillouin echoes distributed sensing technique (BEDS) which leads to a spatial resolution of around 5 cm [66]. Another proposal exceeds this spatial resolution and reaches the sub-mm region by using a frequency modulated source as pump and probe and measuring the Brillouin response of a very narrow correlation peak that can be displaced through the waveguide [67, 68]. The latter is called Brillouin optical correlation domain analysis (BOCDA) and was inspired by similar techniques from the radar community. The principle of this technique relies on a broad source (either frequency modulated, phase modulated or an incoherent source based on amplified spontaneous emission), which is split into counter-propagating pump and probe light, whereby the probe light is down-shifted by the Brillouin frequency shift. The phase of both waves while propagating through the device under test is random, however they exhibit correlation peaks, one exactly in the middle of the experimental setup - the position where the Brillouin interaction is localized and finally measured. The correlation peak can be swept through the device and therefore a distributed Brillouin measurement can be achieved. Such high spatial resolution can give insight into the Brillouin response of short integrated waveguides [69]. Note that all these techniques rely on backward Brillouin scattering. However, recently it has been proposed and experimentally shown that also forward Brillouin scattering can be used for a distributed measurement of the acoustic properties along a waveguide [70–72]. Usually, Brillouin sensors bare the challenge of discrimination of temperature and strain effect on the Brillouin frequency shift. The polarization dependence of Brillouin scattering can help to differentiate these in a polarization maintaining fiber [73].

A variation of the standard backward Brillouin scattering experimental setup can be used for Brillouin-based light storage [13, 14]. The experimental design is again based on the setup in Fig. 12, this time including Module 1 (control pulses) and Module 2 (data pulses). Both pulses - shifted by the Brillouin frequency shift - travel from opposite sides through the waveguide. The power of the data pulses is roughly 10% of the power of the control pulses (frequency down-shifted arm). At the position where they cross, they create an acoustic wave: this can be seen as a writing process, as the information (both amplitude and phase) of the optical waves is transferred to the acoustic wave. This information can be read out with a second so-called read pulse at the frequency down-shifted arm (control arm), and detected at the oscilloscope. This principle leads to a versatile optical delay line and has been demonstrated for its coherent information transfer [14], multi-frequency interaction [74] and

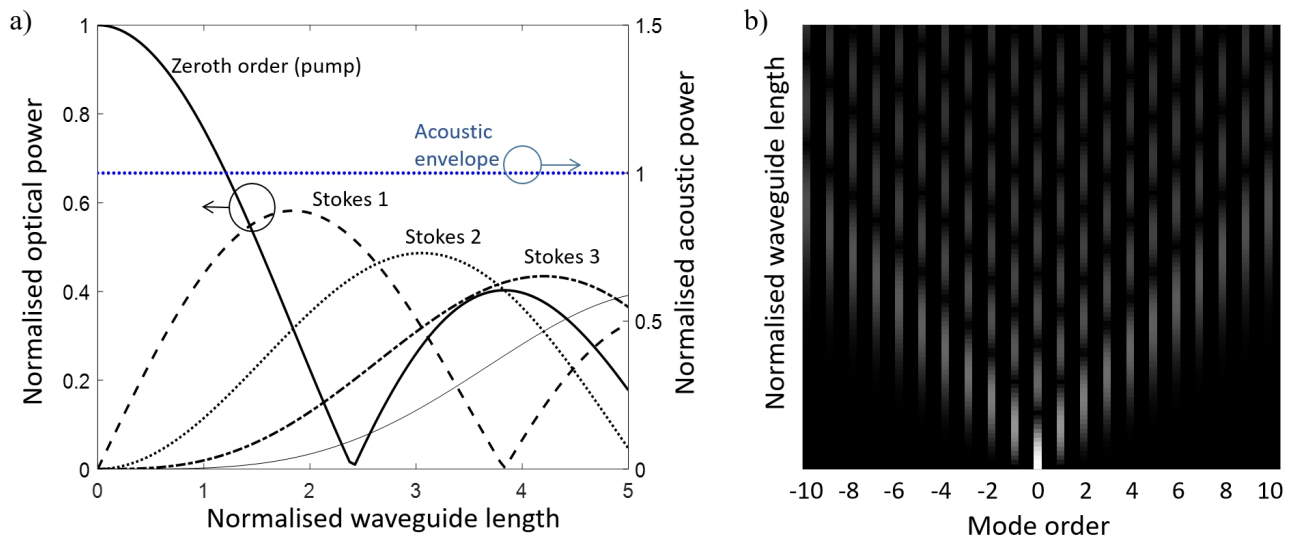


Fig. 10. Evolution of Stokes lines in forward Brillouin scattering. Both (a) and (b) show the power in the pump and Stokes lines, normalised to the input pump power P_{pump} , as a function of the normalised waveguide length $\zeta = z/L_c$ as defined by Eq. 75. In (a) we see that the acoustic mode amplitude is constant throughout the waveguide - this is a result of the fact that in forward Brillouin scattering the acoustic mode is neither amplified nor damped, and modulates the phase of the optical signal. In (b) we see that the Stokes and anti-Stokes lines appear symmetrically about the pump.

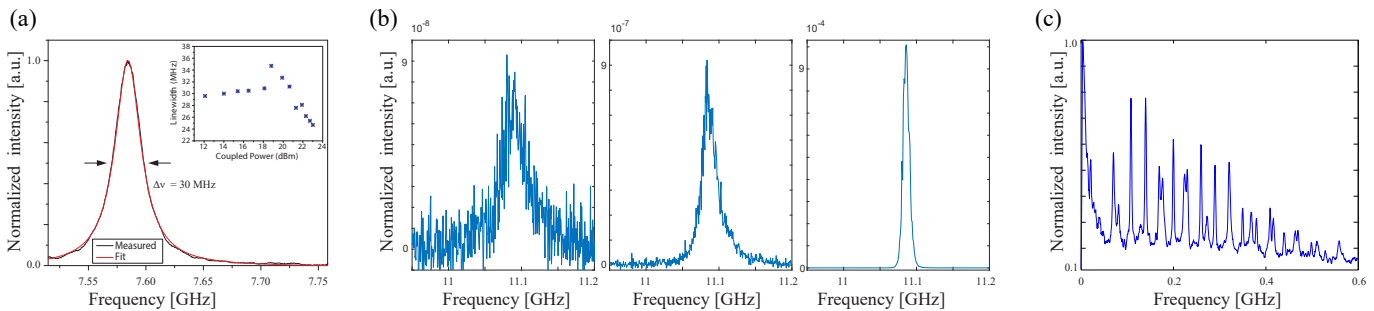


Fig. 11. Experimental data for a) a pump-probe backward SBS setup, chalcogenide integrated waveguide (b) noise-initiated backward SBS setup, from left to right increasing pump power level, silica photonic crystal fiber; (c) noise-initiated forward Brillouin scattering setup, guided acoustic wave Brillouin scattering in 25 m of a standard silica single mode fibre.

the ability of reinforcing acoustic waves [75].

Within Brillouin-based delay techniques quasi-light storage via Brillouin scattering [76] and Brillouin-based slow light [77, 78] have also been demonstrated; an overview can be found in Ref. [79]. Other applications of backward Brillouin scattering are in the fields of narrow-linewidth lasers [8, 80–82], optical and RF filtering and microwave photonics of which recent overviews can be found in Refs. [83–85]. Forward Brillouin scattering has also found several applications, for example in using transverse modes for passive laser mode-locking [86–89], sensing [70–72, 90], Brillouin lasing [8, 91] and emitter-receiver schemes [92].

6. CONCLUSION AND FURTHER READING

Within this article we have covered those aspects of Brillouin scattering that we believe are fundamental to the understanding of the process, from both a theoretical and experimental perspective. However there are a number of important aspects to Brillouin processes that we have not discussed explicitly here.

Of particular importance is the interaction between Brillouin scattering and other nonlinearities. Backward Brillouin scattering can interact in a non-trivial way with the Kerr effect, enhancing nonlinear processes such as four-wave mixing. This is discussed in depth in [93]. A full theoretical treatment of Brillouin scattering, including the Kerr effect, can be found in the Appendix of Winful [94], who once referred to the contained equations as ‘the kitchen sink equations’ because they contain all relevant nonlinear processes and also include optical chirp, which was used in this paper to enhance the efficiency of Brillouin-based acoustic memory. Within semi-conductors, nonlinear loss processes can play an extremely important role. In particular, while two-photon absorption leads to a very small effect, the creation of charge carriers leads to dramatically enhanced nonlinear losses. This in fact puts fixed power limits on the strength of SBS in semiconductors [53].

We have focussed here on simple waveguide geometries, however there is a rich literature studying Brillouin processes in

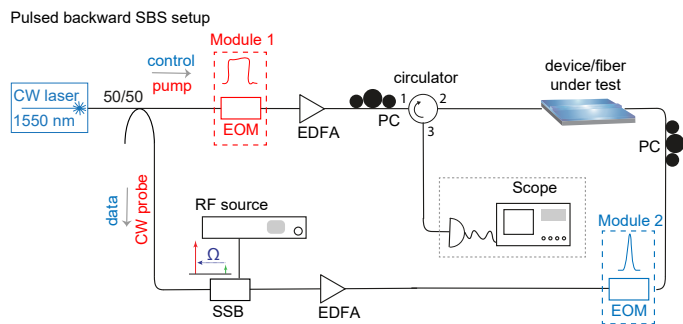


Fig. 12. Pulsed backward Brillouin scattering setup. i) Distributed Brillouin sensor setup; with module 1 but without module 2, this setup resolves the Brillouin interaction spatially with a pulsed pump and CW probe. The amplification of the probe through a pulsed pump is observed at the oscilloscope. ii) Brillouin memory setup; with both modules 1 and 2, this scheme refers to Brillouin dynamic gratings and Brillouin storage. Both interacting waves are pulsed and therefore a local acoustic grating is created. The measurements are observed at the oscilloscope. Components in the setup: EDFA, erbium-doped fiber amplifier; PC, polarization controller; SSB, single-sideband modulator; EOM, electro-optic modulator.

resonators. This is naturally connected to the study of Brillouin lasers, which we have not covered at all. A good introduction to the study of Brillouin scattering in ring resonators can be found in [95]. A general discussion of Brillouin lasing, including the effects of noise, can be found in [96], and a more detailed discussion of noise in integrated Brillouin lasers can be found in [97].

We have also assumed throughout that the Brillouin process takes place in a completely dispersionless environment. By-and-large this is a good approximation, since the Brillouin linewidth is usually sufficiently small, and pulses sufficiently long, that dispersion effects can be safely neglected. However in highly-dispersive waveguides such as multi-structured optical fibres near a band-edge, this assumption may not necessarily hold, and interesting effects may be observed. In particular, the balance between the Stokes and anti-Stokes process in forward Brillouin scattering no longer strictly holds, causing amplification or damping of the acoustic field. A full discussion can be found in [33].

Here we have concentrated on the forward and backward intra-modal processes, however there is much work, and some very interesting physics, in the realm of inter-modal scattering. In particular the papers [98, 99] have comprehensively examined intermodal scattering in photonic crystal fibres, both experimentally and theoretically.

Finally, a particularly interesting aspect of both backward and intermodal Brillouin scattering is that they are inherently non-reciprocal, because the interaction breaks time-reversal symmetry through the creation of an acoustic grating that travels in a particular direction. This effect could be leveraged to create an optical isolator. As with all non-reciprocal devices, a careful distinction should be made between systems that are capable of true isolation, by which is meant a device that blocks any possible backward-propagating state, and those which control the propagation of optical states in a non-reciprocal way [100, 101]. A device that uses Brillouin scattering to drive non-reciprocal

mode-conversion of optical signals which are then selectively filtered would in this sense be a true isolator, being analogous to isolators based on frequency conversion [102]. A proposal for true Brillouin-based isolation was first given in [11], and non-reciprocal Brillouin effects have been demonstrated in recent experimental work [103, 104].

ACKNOWLEDGEMENTS

CW acknowledges funding from a MULTIPLY fellowship under the Marie Skłodowska-Curie COFUND Action (grant agreement No. 713694), the VILLUM FONDEN (grant No. 16498); the Center for Nano Optics is financially supported by the University of Southern Denmark (SDU 2020 funding). MS acknowledges funding from the EPSRC (grant no EP/R014604/1). BS acknowledges funding from the Max Planck Society through an Independent Research Group. CP acknowledges support from the Australian Research Council via Discovery Project DP200101893. We acknowledge our co-workers F. Shuklin, A. Popp and X. Zeng, who gave valuable feedback on the draft. All authors contributed equally and worked together on all parts of the manuscript. Finally, we acknowledge O. Poulton, who did her level best to derail the writing of this manuscript but was ultimately sent to bed.

DISCLOSURES

The authors declare that there are no conflicts of interest related to this article.

REFERENCES

1. R. W. Boyd, *Nonlinear optics* (Academic press, London, 2003), 3rd ed.
2. L. Brillouin, "Diffusion de la lumière et des rayons X par un corps transparent homogène," *Ann. Phys.(Paris)* **17**, 21 (1922).
3. L. Mandelstam, "Light scattering by inhomogeneous media," *Zh. Russ. Fiz.-Khim. Ova* **58**, 381 (1926).
4. B. J. Eggleton, C. G. Poulton, P. T. Rakich, M. J. Steel, and G. Bahl, "Brillouin integrated photonics," *Nat. Photonics* **13**, 664–677 (2019).
5. B. Vidal, M. A. Piqueras, and J. Martí, "Tunable and reconfigurable photonic microwave filter based on stimulated Brillouin scattering," *Opt. Lett.* **32**, 23–25 (2007).
6. D. Marpaung, M. Pagani, B. Morrison, and B. J. Eggleton, "Nonlinear integrated microwave photonics," *J. Light. Technol.* **32** (2014).
7. K. O. Hill, B. S. Kawasaki, and D. C. Johnson, "CW Brillouin laser," *Appl. Phys. Lett.* **28**, 608–609 (1976).
8. N. T. Otterstrom, R. O. Behunin, E. A. Kittlaus, Z. Wang, and P. T. Rakich, "A silicon Brillouin laser," *Science* **360**, 1113–1116 (2018).
9. A. Zarifi, B. Stiller, M. Merklein, Y. Liu, B. Morrison, A. Casas-Bedoya, G. Ren, T. G. Nguyen, K. Vu, D.-Y. Choi, A. Mitchell, S. J. Madden, and B. J. Eggleton, "On-chip correlation-based Brillouin sensing: design, experiment, and simulation," *J. Opt. Soc. Am. B* **36**, 146–152 (2019).
10. M. Nikles, L. Thévenaz, and P. A. Robert., "Simple distributed fiber sensor based on Brillouin gain spectrum analysis," *Opt. Lett.* **21**, 758–760 (1996).
11. X. Huang and S. Fan, "Complete all-optical silica fiber isolator via Stimulated Brillouin Scattering," *J. Light. Technol.* **29**, 2267–2275 (2011).
12. J. Kim, M. C. Kuzyk, K. Han, H. Wang, and G. Bahl, "Non-reciprocal Brillouin scattering induced transparency," *Nat. Phys.* **11**, 275–280 (2015).
13. Z. Zhu, D. J. Gauthier, and R. W. Boyd, "Stored Light in an Optical Fiber via Stimulated Brillouin Scattering," *Science* **318**, 1748–1753 (2007).
14. M. Merklein, B. Stiller, K. Vu, S. J. Madden, and B. J. Eggleton, "A chip-integrated coherent photonic-phononic memory," *Nat. Commun.* **8**, 1–6 (2017).
15. R. Van Laer, R. Baets, and D. Van Thourhout, "Unifying Brillouin scattering and cavity optomechanics," *Phys. Rev. A* **93**, 053828 (2016).

16. G. S. Wiederhecker, P. Dainese, and T. P. Mayer Alegre, "Brillouin optomechanics in nanophotonic structures," *APL Photonics* **4**, 071101 (2019).
17. A. Kobayakov, M. Sauer, and D. Chowdhury, "Stimulated Brillouin scattering in optical fibers," *Adv. Opt. Photonics* **2**, 1–59 (2010).
18. B. A. Auld, *Acoustic fields and waves in solids* (Wiley, New York, 1973).
19. A. Taflov and S. C. Hagness, *Computational electrodynamics: the finite-difference time-domain method; 3rd ed.*, Artech House antennas and propagation library (Artech House, Boston, MA, 2005).
20. D. F. Nelson and M. Lax, "New symmetry for acousto-optic scattering," *Phys. Rev. Lett.* **24**, 379 (1970).
21. D. F. Nelson, *Electric, optic, and acoustic interactions in dielectrics* (John Wiley & Sons, New York, 1979).
22. M. J. A. Smith, C. M. de Sterke, C. Wolff, M. Lapine, and C. G. Poulton, "Enhanced acousto-optic properties in layered media," *Phys. Rev. B* **96**, 064114 (2017).
23. Blundell, Stephen and K. M. Blundell, *Concepts in Thermal Physics* (Oxford University Press, Oxford, UK, 2014), 2nd ed.
24. C. Wolff, M. Steel, B. Eggleton, and C. Poulton, "Stimulated Brillouin scattering in integrated photonic waveguides: Forces, scattering mechanisms, and coupled-mode analysis," *Phys. Rev. A* (2015).
25. P. Rakich, C. Reinke, R. Camacho, P. Davids, and Z. Wang, "Giant enhancement of stimulated Brillouin scattering in the subwavelength Limit," *Phys. Rev. X* **2**, 011008 (2012).
26. H. Shin, W. Qiu, R. Jarecki, J. A. Cox, R. H. Olsson III, A. Starbuck, Z. Wang, and P. T. Rakich, "Tailorable stimulated Brillouin scattering in nanoscale silicon waveguides," *Nat. Commun.* **4**, 1944 (2013).
27. R. Van Laer, B. Kuyken, D. Van Thourhout, and R. Baets, "Interaction between light and highly confined hypersound in a silicon photonic nanowire," *Nat. Photonics* **9**, 199–203 (2015).
28. P. Dainese, P. S. J. Russell, G. S. Wiederhecker, N. Joly, H. L. Fragnito, V. Laude, and A. Khelif, "Raman-like light scattering from acoustic phonons in photonic crystal fiber," *Opt. Express* **14**, 4141–4150 (2006).
29. F.-I. Hsiao, C.-c. Chen, and V. Laude, "Waveguiding inside the complete band gap of a phononic crystal slab," *Phys. Rev. E* pp. 1–6 (2007).
30. R. M. Shelby, M. D. Levenson, and P. W. Bayer, "Guided acoustic-wave Brillouin scattering," *Phys. Rev. B* **31**, 5244–5252 (1985).
31. C. Wolff, M. J. Steel, and C. G. Poulton, "Formal selection rules for Brillouin scattering in integrated waveguides and structured fibers," *Opt. Express* **22**, 32489–32501 (2014).
32. J. E. Sipe and M. J. Steel, "A Hamiltonian treatment of Stimulated Brillouin Scattering in nonlinear integrated waveguides," *New J. Phys.* **18**, 045004:1–21 (2016).
33. C. Wolff, B. Stiller, B. J. Eggleton, M. J. Steel, and C. G. Poulton, "Cascaded forward Brillouin scattering to all Stokes orders," *New J. Phys.* **19**, 023021 (2017).
34. A. B. Shkarin, N. E. Flowers-Jacobs, S. W. Hoch, A. D. Kashkanova, C. Deutsch, J. Reichel, and J. G. E. Harris, "Optically mediated hybridization between two mechanical modes," *Phys. Rev. Lett.* **112**, 013602 (2014).
35. S. G. Johnson, M. Ibanescu, M. A. Skorobogatiy, O. Weisberg, J. D. Joannopoulos, and Y. Fink, "Perturbation theory for Maxwell's equations with shifting material boundaries," *Phys. Rev. E* **65**, 066611 (2002).
36. B. C. P. Sturmberg, K. B. Dossou, M. J. A. Smith, B. Morrison, C. G. Poulton, and M. J. Steel, "Finite element analysis of stimulated Brillouin scattering in integrated photonic waveguides," *J. Light. Technol.* **37**, 3791–3804 (2019).
37. P. Kornreich, H. Callen, and A. Gundjian, "current striction"—a mechanism of electrostriction in many-valley semiconductors," *Phys. Rev.* **161**, 815–822 (1967).
38. K. S. Abedin, "Observation of strong stimulated Brillouin scattering in single-mode As_2Se_3 chalcogenide fiber," *Opt. Express* **13**, 10266–10271 (2005).
39. M. J. A. Smith, B. T. Kuhlmeier, C. M. de Sterke, C. Wolff, M. Lapine, and C. G. Poulton, "Metamaterial control of stimulated Brillouin scattering," *Opt. Lett.* **41**, 2338–2341 (2016).
40. D. K. Biegelsen, "Photoelastic tensor of silicon and the volume dependence of the average gap," *Phys. Rev. Lett.* **32**, 1196 (1974).
41. C. Florea, M. Bashkansky, Z. Dutton, J. Sanghera, P. Pureza, and I. Aggarwal, "Stimulated Brillouin scattering in single-mode As_2S_3 and As_2Se_3 chalcogenide fibers," *Opt. Express* **14**, 12063–12070 (2006).
42. R. K. Galkiewicz and J. Tauc, "Photoelastic properties of amorphous As_2S_3 ," *Solid State Commun.* **10**, 1261–1264 (1972).
43. H. H. Li, "Refractive index of silicon and germanium and its wavelength and temperature derivatives," *J. Phys. Chem. Ref. Data* **9**, 561–658 (1980).
44. H. P. R. Frederikse, "CRC Handbook of Chemistry and Physics, 95th edition," in *Elastic constants of single crystals*, vol. 12 W. M. Haynes, ed. (CRC Press, 2014), pp. 33–38.
45. B. G. Helme and P. J. King, "The phonon viscosity tensor of Si, Ge, GaAs, and InSb," *Phys. Status Solidi A* **45**, K33–K37 (1978).
46. T. Skauli, P. Kuo, K. L. Vodopyanov, T. J. Pinguet, O. Levi, L. A. Eyres, J. S. Harris, M. M. Fejer, B. Gerard, L. Becouarn *et al.*, "Improved dispersion relations for GaAs and applications to nonlinear optics," *J. Appl. Phys.* **94**, 6447–6455 (2003).
47. C. Wolff, R. V. Laer, M. J. Steel, B. J. Eggleton, and C. G. Poulton, "Brillouin resonance broadening due to structural variations in nanoscale waveguides," *New J. Phys.* **18**, 025006 (2016).
48. B. J. Eggleton, C. G. Poulton, and R. Pant, "Inducing and harnessing stimulated Brillouin scattering in photonic integrated circuits," *Adv. Opt. Photonics* **5**, 536–587 (2013).
49. C. G. Poulton, R. Pant, and B. J. Eggleton, "Acoustic confinement and stimulated Brillouin scattering in integrated optical waveguides," *J. Opt. Soc. Am. B* **30**, 2657–2664 (2013).
50. G. G. Gurzadyan and P. Tzankov, "Springer Handbook of Materials Data, 2nd edition," in *Dielectrics and Electrooptics*, vol. 23 H. Warlimont and W. Martienssen, eds. (Springer, 2018), pp. 809–884.
51. K. Bindra, H. Bookey, A. Kar, B. Wherrett, X. Liu, and A. Jha, "Nonlinear optical properties of chalcogenide glasses: Observation of multiphoton absorption," *Appl. Phys. Lett.* **79**, 1939–1941 (2001).
52. Y. Liu and H. Tsang, "Time dependent density of free carriers generated by two photon absorption in silicon waveguides," *Appl. Phys. Lett.* **90**, 211105 (2007).
53. C. Wolff, P. Gutsche, M. J. Steel, B. J. Eggleton, and C. G. Poulton, "Impact of nonlinear loss on stimulated Brillouin scattering," *J. Opt. Soc. Am. B* **32**, 1968 (2015).
54. K. Tanaka, "Photoinduced structural changes in chalcogenide glasses," *Rev. Solid State Sci.* **4**, 641–659 (1990).
55. C. M. de Sterke, K. R. Jackson, and B. D. Robert, "Nonlinear coupled-mode equations on a finite interval: a numerical procedure," *J. Opt. Soc. Am. B* **8**, 403–412 (1991).
56. V. Lanticq, S. Jiang, R. Gabet, Y. Jauouën, F. Taillade, G. Moreau, and G. P. Agrawal, "Self-referenced and single-ended method to measure Brillouin gain in monomode optical fibers," *Opt. Lett.* **34** (2009).
57. O. A. Nieves, M. D. Arnold, M. J. Steel, M. K. Schmidt, and C. G. Poulton, "Noise and Pulse Dynamics in Backward Stimulated Brillouin Scattering," *arXiv* (2020).
58. M. Kang, A. Nazarkin, A. Brenn, and P. S. Russell, "Tightly trapped acoustic phonons in photonic crystal fibres as highly nonlinear artificial Raman oscillators," *Nat. Phys.* **5**, 276–280 (2009).
59. E. M. Dianov, A. V. Luchnikov, A. N. Piliipetskii, and A. N. Starodumov, "Electrostriction mechanism of soliton interaction in optical fibers," *Opt. Lett.* **15**, 314–316 (1990).
60. D. B. Mortimore, "Fiber loop reflectors," *J. Light. Technol.* **6**, 1217–1988 (1988).
61. N. Nishizawa, S. Kume, M. Mori, T. Goto, and A. Miyauchi, "Symmetric and asymmetric fiber loop mirrors for observing guided-acoustic-wave Brillouin scattering in polarization-maintaining fibers," *Opt. Lett.* **19**, 1424–1426 (1994).
62. J.-C. Beugnot, T. Sylvestre, H. Maillotte, G. Mélin, and V. Laude, "Guided acoustic wave Brillouin scattering in photonic crystal fiber," *Nat. Phys.* **5**, 276–280 (2009).
63. B. Stiller, M. Delqué, J.-C. Beugnot, M. W. Lee, G. Mélin, H. Maillotte, V. Laude, and T. Sylvestre, "Frequency-selective excitation of guided acoustic modes in a photonic crystal fiber," *Opt. Express* **19**, 7689–7694 (2011).

64. L. Thévenaz, "Brillouin distributed time-domain sensing in optical fibers: state of the art and perspectives," *Front. Opt. China* **3**, 13 (2010).
65. C. A. Galindez-Jamioy and J. M. Lopez-Higuera, "Brillouin Distributed Fiber Sensors," *J. Sensors* (2012).
66. S. M. Foaleng, M. Tur, J.-C. Beugnot, and L. Thévenaz, "High spatial and spectral resolution long-range sensing using Brillouin echoes," *J. Light. Technol.* **28**, 2993–3003 (2010).
67. K. Hotate and T. Hasegawa, "Measurement of Brillouin gain spectrum distribution along an optical fiber using a correlation-based technique - proposal, experiment and simulation," *IEICE Trans. Electron.* **83-C**, 405–412 (2000).
68. R. Cohen, Y. London, Y. Antman, and A. Zadok, "Brillouin optical correlation domain analysis with 4 millimeter resolution based on amplified spontaneous emission," *Opt. Express* **22** (2014).
69. A. Zarifi, B. Stiller, M. Merklein, and B. Eggleton, "High resolution Brillouin sensing of micro-scale structures," *Appl. Sci.* **8**, 2572 (2018).
70. C. Pang, Z. Hua, D. Zhou, H. Zhang, L. Chen, X. Bao, and Y. Dong, "Opto-mechanical time-domain analysis based on coherent forward stimulated Brillouin scattering probing," *Optica* **7** (2020).
71. G. Bashan, H. H. Diamandi, Y. London, E. Preter, and A. Zadok, "Optomechanical time-domain reflectometry," *Nat. Commun.* **9** (2018).
72. D. M. Chow, Z. Yang, M. A. Soto, and L. Thévenaz, "Distributed forward Brillouin sensor based on local light phase recovery," *Nat. Commun.* **9** (2018).
73. W. Zou, Z. He, and K. Hotate, "Complete discrimination of strain and temperature using Brillouin frequency shift and birefringence in a polarization-maintaining fiber," *Opt. Express* **17** (2009).
74. B. Stiller, M. Merklein, K. Vu, P. Ma, S. J. Madden, C. G. Poulton, and B. J. Eggleton, "Cross talk-free coherent multi-wavelength Brillouin interaction," *APL Photonics* **4** (2019).
75. B. Stiller, M. Merklein, C. Wolff, K. Vu, P. Ma, S. J. Madden, and B. J. Eggleton, "Coherently refreshing hypersonic phonons for light storage," *Optica* **7** (2020).
76. S. Preußler, K. Jamshidi, A. Wiatrek, R. Henker, C.-A. Bunge, and T. Schneider, "Quasi-light-storage based on time-frequency coherence," *Opt. Express* **17** (2009).
77. Y. Okawachi, M. S. Bigelow, J. E. Sharping, Z. Zhu, A. Schweinsberg, D. J. Gauthier, R. W. Boyd, and A. L. Gaeta, "Tunable all-optical delays via Brillouin slow light in an optical fiber," *Phys. Rev. Lett.* **94** (2005).
78. K. Y. Song, M. G. Herraes, and L. Thévenaz, "Observation of pulse delaying and advancement in optical fibers using stimulated Brillouin scattering," *Opt. Express* **13** (2005).
79. M. Merklein, B. Stiller, and B. J. Eggleton, "Brillouin-based light storage and delay techniques," *J. Opt. (United Kingdom)* **20** (2018).
80. K. O. Hill, B. S. Kawasaki, and D. C. Johnson, "cw Brillouin laser," *Appl. Phys. Lett.* **28** (1976).
81. I. V. Kabakova, R. Pant, D.-Y. Choi, S. Debbarma, B. Luther-Davies, S. J. Madden, and B. J. Eggleton, "Narrow linewidth Brillouin laser based on chalcogenide photonic chip," *Opt. Lett.* **38** (2013).
82. S. Gundavarapu, G. M. Brodnik, M. Puckett, T. Huffman, D. Bose, R. Behunin, J. Wu, T. Qiu, C. Pinho, N. Chauhan, J. Nohava, P. T. Rakich, K. D. Nelson, M. Salit, and D. J. Blumenthal, "Sub-hertz fundamental linewidth photonic integrated Brillouin laser," *Nat. Photonics* **13** (2019).
83. M. Merklein, A. Casas-Bedoya, D. Marpaung, T. F. Buttner, M. Pagani, B. Morrison, I. V. Kabakova, and B. J. Eggleton, "Stimulated Brillouin Scattering in Photonic Integrated Circuits: Novel Applications and Devices," *IEEE J. Sel. Top. Quantum Electron.* **22** (2016).
84. A. Choudhary, Y. Liu, D. Marpaung, and B. J. Eggleton, "On-Chip Brillouin Filtering of RF and Optical Signals," *IEEE J. Sel. Top. Quantum Electron.* **24** (2018).
85. Y. Liu, A. Choudhary, D. Marpaung, and B. J. Eggleton, "Integrated microwave photonic filters," *Adv. Opt. Photonics* **12** (2020).
86. M. S. Kang, N. Y. Joly, and P. S. J. Russell, "Passive mode-locking of fiber ring laser at the 337th harmonic using gigahertz acoustic core resonances," *Opt. Lett.* **38** (2013).
87. B. Stiller and T. Sylvestre, "Observation of acoustically induced modulation instability in a Brillouin photonic crystal fiber laser," *Opt. Lett.* **38** (2013).
88. M. Pang, X. Jiang, W. He, G. K. L. Wong, G. Onishchukov, N. Y. Joly, G. Ahmed, C. R. Menyuk, and P. S. Russell, "Stable subpicosecond soliton fiber laser passively mode-locked by gigahertz acoustic resonance in photonic crystal fiber core," *Optica* **2** (2015).
89. W. He, M. Pang, C. R. Menyuk, and P. S. J. Russell, "Sub-100-fs 187 GHz mode-locked fiber laser using stretched-soliton effects," *Optica* **3** (2016).
90. E. Carry, J. C. Beugnot, B. Stiller, M. W. Lee, H. Maillotte, and T. Sylvestre, "Temperature coefficient of the high-frequency guided acoustic mode in a photonic crystal fiber," *Appl. Opt.* **50** (2011).
91. B. Morrison, A. Casas-Bedoya, G. Ren, K. Vu, Y. Liu, A. Zarifi, T. G. Nguyen, D. Y. Choi, D. Marpaung, S. Madden, A. Mitchell, and B. J. Eggleton, "Compact Brillouin devices through hybrid integration on silicon," (2017).
92. H. Shin, J. A. Cox, R. Jarecki, A. Starbuck, Z. Wang, and P. T. Rakich, "Control of coherent information via on-chip photonic-phononic emitter-receivers," *Nat. Commun.* **6** (2015).
93. A. M. Scott and K. D. Ridley, "A Review of Brillouin-Enhanced Four-Wave Mixing," *IEEE J. Quantum Electron.* **25**, 438–459 (1989).
94. H. G. Winful, "Chirped Brillouin dynamic gratings for storing and compressing light," *Opt. Express* **21**, 10039–10047 (2013).
95. S. R. Mirnaziry, C. Wolff, M. J. Steel, B. J. Eggleton, and C. G. Poulton, "Stimulated Brillouin scattering in integrated ring resonators," *J. Opt. Soc. Am. B* **34**, 937–949 (2017).
96. T. Buettner, "Brillouin Frequency Comb Generation in Chalcogenide Waveguides," Ph.D. thesis, University of Sydney (2015).
97. R. O. Behunin, N. T. Otterstrom, P. T. Rakich, S. Gundavarapu, and D. J. Blumenthal, "Fundamental noise dynamics in cascaded-order Brillouin lasers," *Phys. Rev. A* **98**, 023832 (2018).
98. A. Butsch, J. R. Koehler, R. E. Noskov, and P. S. Russell, "CW-pumped single-pass frequency comb generation by resonant optomechanical nonlinearity in dual-nanoweb fiber," *Optica* **1**, 158–164 (2014).
99. J. R. Koehler, R. E. Noskov, A. A. Sukhorukov, A. Butsch, D. Novoa, and P. S. J. Russell, "Resolving the mystery of milliwatt-threshold optomechanical self-oscillation in dual-nanoweb fiber," *APL Photonics* **1**, 056101 (2016).
100. D. Jalas, A. Petrov, M. Eich, W. Freude, S. Fan, Z. Yu, R. Baets, M. Popović, A. Melloni, J. D. Joannopoulos, M. Vanwolleghem, C. R. Doerr, and H. Renner, "What is — and what is not — an optical isolator," *Nat. Photonics* **7**, 579–582 (2013).
101. J. B. Khurgin, "Non-reciprocal propagation versus non-reciprocal control," *Nat. Photonics* **14**, 711–711 (2020).
102. K. Abdelsalam, T. Li, J. B. Khurgin, and S. Fatthpour, "Linear isolators using wavelength conversion," *Optica* **7**, 209–213 (2020).
103. E. A. Kittlaus, N. T. Otterstrom, P. Kharel, S. Gertler, and P. T. Rakich, "Non-reciprocal interband Brillouin modulation," *Nat. Photonics* **12**, 613–619 (2018).
104. M. Merklein, B. Stiller, K. Vu, P. Ma, S. J. Madden, and B. J. Eggleton, "On-chip broadband nonreciprocal light storage," *Nanophotonics* (2020).

A. APPENDIX: COMPUTATION OF ACOUSTIC MODES AND GAIN/COUPLING PARAMETERS

In order to solve the systems of coupled PDEs (such as Eq. (64)) it is first necessary to compute important quantities such as the gain (coupling) coefficient g_0 , frequency shift $\Omega/(2\pi)$, and Brillouin linewidth $\Gamma_b/(2\pi)$. To do this one must accurately compute the fields of both electromagnetic and acoustic modes in the waveguide, given by equations Eq. (12) and Eq. (35) respectively:

$$(\mathbf{D}^{(\text{opt})} + ik_n \mathbf{P}^{(\text{opt})}) |\Psi_n\rangle = i\omega_n \mathbf{E}^{(\text{opt})} |\Psi_n\rangle. \quad (78a)$$

$$(\mathbf{D}^{(\text{ac})} + iq \mathbf{P}^{(\text{ac})}) |\Phi\rangle = i\Omega \mathbf{E}^{(\text{ac})} |\Phi\rangle, \quad (78b)$$

To be properly-defined eigenvalue problems these equations must have appropriate boundary conditions on the edge of the

Waveguide	k_0	n_{eff}	$\frac{\Omega}{2\pi}$	$\frac{\Gamma_b}{2\pi}$	g_0
Si (200 x 450 nm ²)	8.651	2.134	17.29	14.33	-2192
SiO ₂ (1 μm diam.)	4.769 [†]	1.176	9.22	10.65	-26

Table 2. Summary table of backward stimulated Brillouin scattering results for a selection of waveguides, where k_0 denotes the optical wave number with † denoting a degenerate optical mode (in units [10⁶/m]), n_{eff} the effective refractive index, $\Omega/(2\pi)$ the acoustic frequency (in units [GHz]), $\Gamma_b/(2\pi)$ the acoustic linewidth (in units [MHz]), and g_0 denotes the gain (in units [W⁻¹m⁻¹]). Note that gain values are negative-valued as the Stokes wave is backwards propagating.

computational domain. Given that one is typically looking for guided modes, it is usually sufficient to take the edge of the computational domain sufficiently far away and to enforce a perfect conducting condition — or a perfectly clamped condition, in the case of acoustic modes — on the outermost boundary of the domain. For free-standing acoustic structures (e.g. a pedestal waveguide in air) it is sufficient to limit to computational domain to the waveguide itself, and then apply freely-vibrating boundary conditions at the air interface. The problems encompassing the differential equations Eq. (78) together with their boundary conditions are then generalised eigenvalue problems, with the eigenvalue being either the wave number (k_n, q) or the frequency (ω_n, Ω).

The leading approach to solving these equations is by using the Finite Element Method (FEM), for which there are a number of commercially-available solvers. For the following computations we have used a free FEM-based program known as NumBAT, the *Numerical Brillouin Analysis Tool* which is specifically designed for Brillouin problems, and which has been tested against a selection of experimental and numerical results from across the Brillouin scattering literature. The program uses a Python front end, which connects to a fast Fortran solver for constructing a two-dimensional FEM solution for both electromagnetic and acoustic modes. A range of (tutorial-type) scripts for calculating the Brillouin scattering performance of a photonic structure have already been created in the NumBAT installation files and can be modified to suit the needs of the reader. NumBAT code for the results presented in this Appendix are packaged with the latest release. The NumBAT package is available for download at <https://github.com/michaeljsteel/NumBAT>, and the associated documentation suite is also available online at <https://numbat-au.readthedocs.io/en/latest/>. An article highlighting the package and summarising a smaller selection of benchmarks for backward, forward, and intermodal forward Brillouin scattering is available [36].

Regardless of the software chosen to compute the modes, the approach to computing the Brillouin gain/coupling takes the same general form. For backward Brillouin scattering, the procedure is as follows: first calculate the available electromagnetic states in the structure using an estimate for the effective mode index at the pump wavelength (e.g., $\lambda = 1550$ nm). An initial estimate for the effective index of the EM mode can be made by selecting a value close to the refractive index of the waveguide material (NumBAT does this by default). Having determined the available EM states, one must choose which one is the pump field — typically this is the fundamental linearly polarized mode in either the x or y direction, depending on the

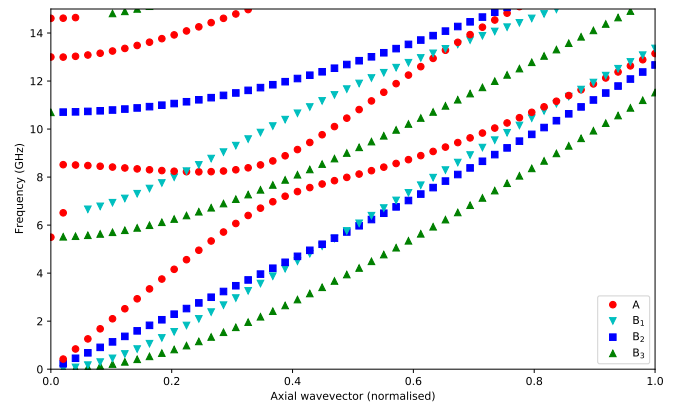


Fig. 13. Elastic dispersion curves for 450 x 200 nm² rectangular Si waveguide obtained using NumBAT. Curves are classified by (irreducible) group representations A , B_1 , B_2 , and B_3 .

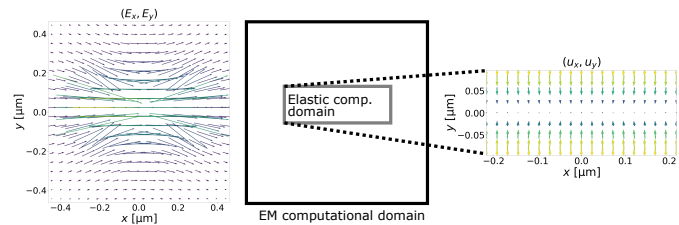


Fig. 14. Transverse optical (pump and Stokes) fields and transverse elastic field profiles for 450 x 200 nm² rectangular Si waveguide corresponding to largest backward SBS gain, calculated using NumBAT. Values are summarised in Table 2 and outlines of computational domains are superposed for reference.

waveguide. For backward scattering, the Stokes field is simply the conjugate of the pump, and because the pump and Stokes frequencies are extremely close, the Stokes wave vector is simply the negative of the pump wave vector. The wave vector q for the elastic field is therefore twice that of the pump following conservation of momentum, in accordance with Eq. (1). The next step is to solve for the available elastic states in the structure, choosing q as a fixed parameter and solving for the eigenvalue Ω . This will typically give a range of solutions, corresponding to all the different possible acoustic frequencies that can couple the pump and Stokes. With both electromagnetic and acoustic fields computed, it is possible to compute the overlaps $Q_{nm'}$ for all elastic modes for the chosen pump and Stokes fields. One quantity that is difficult to predict in advance is the viscoelastic loss. If the components of the viscoelastic loss tensor are known, then these can be inserted into Eq. (46) to compute the overall acoustic loss. In practical situations, it is often more convenient to estimate the linewidth directly from an experiment or from the known phonon lifetime. The modal power \mathcal{P}_p of the pump/Stokes, and the modal energy \mathcal{E}_n , can be computed directly from the field values of the eigenmodes. The gain or coupling coefficients for each acoustic mode can then be computed these quantities in conjunction with $Q_{nm'}$ replacing Q in Eq. (66).

In a typical computation a large number of acoustic eigenmodes are found (in fact, most FEM solvers will allow the user to specify the number of modes to look for). Some of these solutions are symmetry-forbidden and will have zero coupling, how-

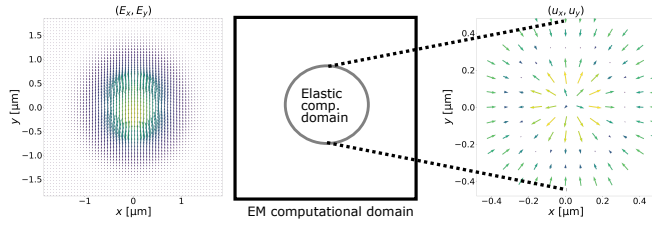


Fig. 15. Transverse optical (pump and Stokes) fields and transverse elastic field profiles for 1 μm diameter circular SiO_2 waveguide corresponding to largest backward SBS gain, calculated using NumBAT. Values are summarised in Table 2 and out-lines of computational domains are superposed for reference.

Waveguide	k_0	n_{eff}	$\frac{\Omega}{2\pi}$	$\frac{\Gamma_b}{2\pi}$	g_0
Si (200 x 450 nm ²)	8.651	2.134	8.52	7.89	17579
SiO_2 (1 μm diam.)	4.769 [†]	1.176	2.81	0.26	174

Table 3. Summary table of forward stimulated Brillouin scattering results; format as in Table. 2.

ever in others the coupling is simply small. Having determined gain values for all of the elastic states, the dominant acoustic mode is readily identified from inspection of the gain values, and all other corresponding constants are easily extracted.

Output values for backward SBS in a rectangular silicon waveguide and for a cylindrical silica waveguide is given in Table 2, showing a significant disparity in gain values. In Figure 13 we profile the elastic dispersion curves for the silicon rectangular waveguide. The corresponding field distributions for the results in Table 2 are shown in Figures 14 and 15.

The approach for computing forward Brillouin scattering is very similar to that for backward Brillouin scattering: the same gain expression g_0 is used (although this quantity becomes a coupling coefficient in place of a gain) and the same electromagnetic field calculations are made to determine the pump field. The key difference is that the Stokes field is not the conjugate of the pump field and the Stokes wave vector is not the negative of the pump wave vector. Here, the elastic wave vector can be, to an excellent approximation, taken to be zero. As in the backward Brillouin scattering case, the acoustic wave vector $q \approx 0$ gives a selection of available elastic fields, and therefore, a range of overlaps and coupling values. A summary of output values for our two waveguide designs are given in Table 3, showing an enhancement in coupling values compared to the gains calculated for the backward configuration. The fields associated with these gain values are presented in Figure 16.

The calculation for intermodal forward Brillouin scattering is slightly different to that of either backward or Forward scattering. Here, the pump and Stokes fields do not refer to the same EM mode index (i.e., for intermodal forward scattering the pump could be the second available EM mode and the Stokes the third available EM mode), and that the elastic wave vector must be explicitly determined following the conservation of momentum condition $q = k_n - k_{n'}$. Nevertheless the approach is the same: having chosen the desired pump and Stokes modes, one is then able to then able to calculate the available elastic modes associated with each value of q , together with all associated gain values. A summary of values for our two waveguide designs is

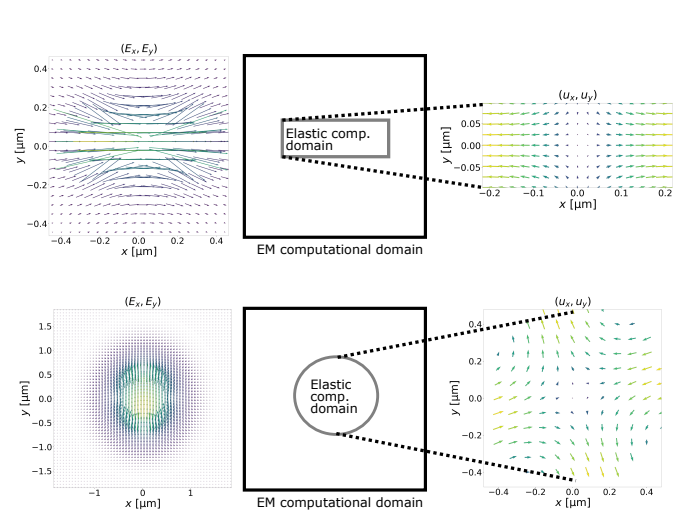


Fig. 16. Transverse optical (pump and Stokes) fields and transverse elastic field profiles corresponding to largest forward SBS coupling for the geometries introduced in Fig. 14 (top row) and Fig. 15 (bottom row), respectively.

Waveguide	k_0	n_{eff}	$\frac{\Omega}{2\pi}$	$\frac{\Gamma_b}{2\pi}$	g_0
Si (200 x 450 nm ²)	8.671	2.134			
	4.29	1.057	2.84	0.43	62724
SiO_2 (1 μm diam.)	4.769 [†]	1.176			
	4.769 [†]	1.176	2.81	0.27	51

Table 4. Summary table of intermodal forward stimulated Brillouin scattering results; format as in Table. 2.

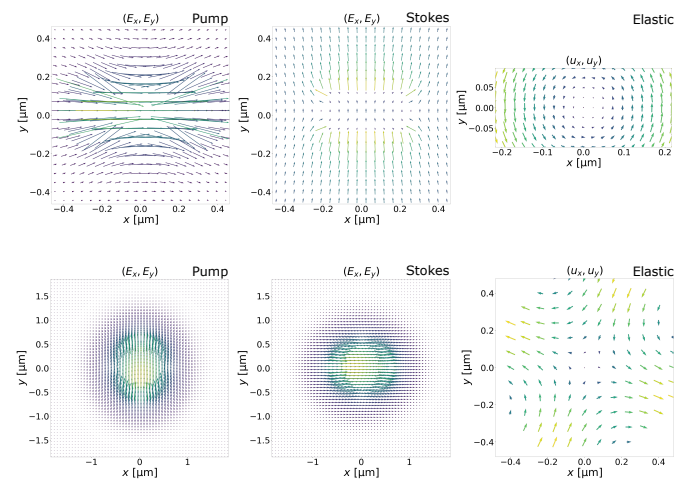


Fig. 17. Transverse optical (pump and Stokes) fields and transverse elastic field profiles corresponding to the largest inter-modal coupling for the geometries introduced in Fig. 14 (top row) and Fig. 15 (bottom row), respectively.

given in Table 4, showing a significant enhancement in the gain for the rectangular silicon waveguide, relative to either the backward gain or forward coupling values presented earlier. This enhancement stems largely from a considerably lower acoustic linewidth. The associated fields for the gain values in Table 4 are presented in Figure 17.